A positive-weight Next-to-Leading Order Monte Carlo simulation for Higgs boson production

A positive-weight Next-to-Leading Order Monte Carlo simulation for Higgs boson production

Keith Hamilton,[a] **Peter Richardson**[b] **and Jon Tully**[b]

[a]*Centre for Particle Physics and Phenomenology (CP3), Université Catholique de Louvain,*
Chemin du Cyclotron 2, 1348 Louvain-la-Neuve, Belgium

[b]*Institute of Particle Physics Phenomenology, Department of Physics,*
University of Durham, Durham, DH1 3LE, U.K.

E-mail: keith.hamilton@uclouvain.be, peter.richardson@durham.ac.uk,
j.m.tully@durham.ac.uk

ABSTRACT: In this article we describe simulations of Higgs boson production via the gluon fusion and Higgs-strahlung processes, using the positive weight next-to-leading-order (NLO) matching scheme, POWHEG, in the Herwig++ 2.3 event generator. This formalism consistently incorporates the full NLO corrections to these processes within the parton shower simulation, without the production of negative weight events. These simulations include a full implementation of the truncated shower required to correctly model soft emissions in an angular-ordered parton shower. We present a thorough validation of these simulations, comparing them to other methods and calculations. The results obtained for the gluon fusion process corroborate, and provide detailed explanations for, findings reported by Alioli *et al* using an independent POWHEG simulation, neglecting truncated shower effects, released at the same time as our code.

Contents

1 Introduction

The primary objective of the ongoing and imminent physics programmes at the Tevatron and LHC, is to elucidate the nature of electroweak symmetry breaking. The great majority of the effort in this direction is devoted to the hunt for the Higgs boson, the origin of this symmetry breaking in the Standard Model (SM) [1–4].

Of all the ways in which the SM Higgs boson can be produced, the gluon fusion process [5], in which it couples to colliding gluons via a top quark loop, has the largest cross section for Higgs boson masses less than $\sim$1 TeV. This process is of great importance for the detection of the Higgs boson at the Tevatron and, more so, at the LHC, particularly in the low mass region, favoured by the latest fits of the Standard Model to electroweak precision data [6], where the decay of the Higgs boson into two photons is known to give a

clean experimental signal. Although observing a narrow resonance in the diphoton invariant mass spectrum should be possible using only the experimental data [7], determining the quantum numbers and couplings of the resonance i.e. determining that it really is a fundamental scalar and, moreover, the SM Higgs boson, will involve a comprehensive analysis of a number of channels, using accurate, flexible, Monte Carlo simulations to predict distributions for signals and backgrounds.

A key part of that identification procedure will be the measurement the couplings of the Higgs boson to the weak gauge bosons and the top quark. Although the gluon fusion process directly probes the latter, associated QCD radiation renders it a significant background to the vector boson fusion process (VBF), in which the Higgs boson originates from HWW and HZZ vertices. Precise simulations of the gluon fusion process are then also required to model the extent to which these events contaminate the VBF signal [8–10].

Another direct probe of Higgs boson interactions with electroweak gauge bosons is the *Higgs-strahlung* process [11, 12]. At leading order this consists of a quark anti-quark annihilation producing a virtual vector boson ($V = W/Z$), which becomes on-shell by radiating a Higgs boson. This channel is particularly important for Higgs boson searches at the Tevatron [13]. The cross section for Higgs-strahlung processes at the LHC is approximately one order of magnitude larger than at the Tevatron, however, the backgrounds scale up by a much greater factor. In spite of these difficulties the Higgs-strahlung processes can still be observed, notably in the $\gamma\gamma$ and W^+W^- decay channels, where significant background rejection can be achieved (see for example ref. [14] for recent experimental studies). Interest in the $b\bar{b}$ plus leptons decay channel has also recently been revived through the observation that a highly collimated $b\bar{b}$ jet, from a boosted Higgs boson, could provide a clean signature [15, 16]. These processes were recommended for inclusion in studies to determine Higgs boson couplings in ref. [17]. As with the gluon fusion process, accurate Monte Carlo simulations will be central to such studies.

Lately combined Tevatron analyses of the gluon fusion and Higgs-strahlung channels have begun to show sensitivity to Higgs boson production [18]. Presently these studies exclude, at the 95% confidence level, the existence of a SM Higgs boson with a mass in the range 160 - 170 GeV. This exclusion limit largely follows from analysis of the gluon fusion channel in which the Higgs decays into a W^+W^- pair. Monte Carlo simulations of Higgs-strahlung and gluon fusion processes were essential in obtaining these measurements.

In recent years research in Monte Carlo simulations has seen major progress, most significantly in the extension of existing parton shower simulations to consistently include exact next-to-leading order corrections [19–34] and, separately, in the consistent combination of parton shower simulations and high multiplicity tree-level matrix element generators [35–40]. The first successful NLO matching scheme was MC@NLO [19–24] which has been realised using the HERWIG event generator for many processes. This method has two draw backs; first, it involves subtracting the parton shower approximation from the NLO calculation, which can lead to unphysical negative weight events, second, the implementation of the method is fundamentally dependent on the details of the parton shower algorithm. In 2004 a new formalism known as POWHEG (POsitive Weight Hardest Emission Generator [26]) was derived, achieving the same aims as MC@NLO but with the

added benefits of only generating physical, positive weight, events as they occur in nature, and of being independent of the details of the parton shower algorithm. This method has been already successfully applied to a number of phenomenologically important processes [25, 27, 30–34, 41, 42].

In this paper we describe the application of the POWHEG method to Monte Carlo simulations for Higgs boson production via gluon fusion and Higgs-strahlung processes, within the Herwig++ [43, 44] event generator. We include a complete description of truncated shower effects.[1] Our primary aim is to present the ingredients used in the simulations and to validate them, where appropriate, against existing calculations.

The structure of the paper is as follows. In section 2 we briefly review the main features of the POWHEG method. In section 3 we collect the essential formulae relating to the NLO cross sections, for implementation in the program. In section 4 we give details of the event generation process for the hard configurations. This is accompanied by a description of how the hard configurations are subsequently reproduced by the angular-ordered parton shower, including truncated showering effects, in respect of the colour coherence phenomenon manifest in soft wide angle gluon emissions. In section 5 we present the results of our implementation, comparing it to the MCFM and MC@NLO generators, before summarizing our findings in section 6.

2 The POWHEG formalism

The central formula in the POWHEG approach is derived by manipulating and modifying, through the inclusion of formally higher order terms, the NLO differential cross section, such that it has the same form as that given by the parton shower [26]. For a given N-body process this is

$$\mathrm{d}\sigma = \overline{B}\left(\Phi_B\right)\mathrm{d}\Phi_B\left[\Delta_{\hat{R}}\left(0\right) + \frac{\widehat{R}\left(\Phi_B, \Phi_R\right)}{B\left(\Phi_B\right)}\Delta_{\hat{R}}\left(k_T\left(\Phi_B, \Phi_R\right)\right)\mathrm{d}\Phi_R\right], \qquad (2.1)$$

where $\overline{B}\left(\Phi_B\right)$ is defined as

$$\overline{B}\left(\Phi_B\right) = B\left(\Phi_B\right) + V\left(\Phi_B\right) + \int \mathrm{d}\Phi_R\left[\widehat{R}\left(\Phi_B, \Phi_R\right) - \sum_i C_i\left(\Phi_B, \Phi_R\right)\right], \qquad (2.2)$$

with $B\left(\Phi_B\right)$ the leading-order contribution, dependent on the *Born variables*, Φ_B, which specify a point in the N-body phase space. $V\left(\Phi_B\right)$ is a finite contribution arising from the combination of unresolvable, real emission and virtual loop corrections. The remaining terms are due to the $N+1$-body real emission processes, hence they have an additional dependence on the *radiative variables*, Φ_R, which parametrize the phase space associated with the extra parton. The real emission term, $\widehat{R}\left(\Phi_B, \Phi_R\right)$, is given by the product of the parton flux factors with the relevant squared real emission matrix element, summed

---

[1]Currently, only the Herwig++ POWHEG simulation of the Drell-Yan process includes a complete treatment of truncated shower effects [32].

over each channel contributing to the NLO cross section. $C_i(\Phi_B, \Phi_R)$ denotes a combination of *real counterterms/counter-event weights*, regulating the singularities in $\widehat{R}(\Phi_B, \Phi_R)$. Finally, the POWHEG Sudakov form factor, $\Delta_{\hat{R}}$, is defined as

$$\Delta_{\hat{R}}(p_T) = \exp\left[-\int d\Phi_R \frac{\widehat{R}(\Phi_B, \Phi_R)}{B(\Phi_B)} \theta(k_T(\Phi_B, \Phi_R) - p_T) \right], \qquad (2.3)$$

where $k_T(\Phi_B, \Phi_R)$ tends to the transverse momentum of the emitted parton in the soft and collinear limits.

To $\mathcal{O}(\alpha_S)$ eq. (2.1) is just the usual NLO differential cross section. The analogous parton shower expression is given by replacing $\overline{B}(\Phi_B) \to B(\Phi_B)$ and the real emission corrections $\widehat{R}(\Phi_B, \Phi_R)$ by their collinear approximation, i.e. replacing the argument of the Sudakov form factor by a sum of Altarelli-Parisi kernels. Typically parton shower simulations generate an N-body configuration according to $B(\Phi_B)$ and then shower it using such a Sudakov form factor. In the POWHEG formalism the initial N-body configuration is instead generated according to $\overline{B}(\Phi_B)$, and retained with probability $\Delta_{\hat{R}}(0)$ as a *non-radiative* event, or, showered to give the hardest emission with $p_T = k_T(\Phi_B, \Phi_R)$, with probability $\Delta_{\hat{R}}(p_T)$ (eq. (2.1)). Further, lower p_T, emissions represent terms of next-to-next-to-leading-order (NNLO) and beyond, hence we can return to the usual parton shower formulation to simulate these. Provided the perturbative approach is valid, i.e. provided the next-to-leading order terms are smaller than the leading order ones, it is clear from eq. (2.2) that $\overline{B}(\Phi_B)$ is positive, therefore no negative weights arise.

Furthermore, it is well known that when a bunch of collimated QCD charges emit a gluon at wide angle, the intensity of the radiation is proportional to the *coherent sum* of emissions from the constituents, *viz.* the jet parent. This effect is manifest in the perturbative series as large soft logarithms. The other major triumph of the POWHEG [26] approach, besides avoiding negative weights, is in rigorously decomposing the angular-ordered parton shower into a *truncated shower*, describing soft wide angle radiation, the *hardest emission*, as described above, and a further *vetoed shower* comprised of lower p_T, increasingly collinear emissions.

We implement the POWHEG formalism in fullness according to the following procedure:

- generate N- and $N+1$-body configurations according to eq. (2.1);

- directly hadronize any N-body, non-radiative, events;

- map the radiative variables parametrizing the emission into the evolution scale, momentum fraction and azimuthal angle $(\tilde{q}_h, z_h, \phi_h)$, from which the parton shower would reconstruct identical momenta;

- take the initial N-body configuration, Φ_B, generated from $\overline{B}(\Phi_B)$, and evolve the emitting leg from the default initial scale down to $\tilde{q}_h$ using the truncated shower;

- insert a branching with parameters $(\tilde{q}_h, z_h, \phi_h)$ into the shower when the evolution scale reaches $\tilde{q}_h$;

- generate p_T vetoed showers from all external legs.

3 Next-to-Leading Order cross sections

The NLO ingredients needed to implement the POWHEG method for Higgs-strahlung processes can be performed in the same way as ref. [32] due to the careful organization of the Drell-Yan differential cross section in our earlier work. There we explicitly factorized the real emission corrections to the leading-order $q + \bar{q} \to l + \bar{l}$ process at the level of the phase space *and* the real emission matrix elements. This meant that the radiative variables could be generated completely independently from the details of the decay of the off-shell vector boson. We refer the reader to ref. [32] for details of those matrix elements.

Since the diagrams involved in the NLO corrections to Drell-Yan and Higgs-strahlung processes are identical up to replacing the final-state lepton pair with a vector boson and a Higgs boson, the factorized NLO differential cross section is exactly the same as that in ref. [32] for the Drell-Yan process; one simply replaces the $q + \bar{q} \to l + \bar{l}$ leading-order matrix element with that for $q + \bar{q} \to V + H$ throughout. No information regarding spin correlations is lost in this procedure and the full NLO distribution is generated without approximation. This method is originally due to Kleiss [45, 46] and was extended for use in our POWHEG simulation, with a view to making other processes easier to implement. Due to the complexity of the 4-body final state (we include the decays of V and H) and the subtleties of the Monte Carlo algorithm, we have carried out detailed comparisons against the parton level NLO simulation MCFM [47]. Results of these comparisons are given later in section 5.

The NLO cross section for Higgs boson production via gluon fusion was first calculated in refs. [48, 49], in the infinite top-quark mass limit. Later this calculation was improved to exactly include the effects of the finite top mass in [50], where it was found that the infinite top-quark mass limit provided an excellent approximation to the full result; below the $t\bar{t}$ threshold the exact and approximate calculations agree at the level of 10% [7]. In the last decade the NNLO corrections were also fully computed by three independent groups, in the infinite top-quark mass limit [51–54]. More recently a parton level Monte Carlo program accurate to NNLO has become available [55, 56]. A key point arising from this theoretical activity is that the dominant perturbative corrections to the total cross section originate from virtual and soft-gluon corrections, which explains the surprising accuracy of the infinite top-quark mass approximation for $m_H \leq 2m_t$ [57].

In our simulation we use the infinite top-quark mass limit. Although the NLO formulae in [48, 49] are helpful, they were only used to compute the most inclusive of measurements, namely the total cross section. Further work is needed to obtain a form suitable for a fully differential Monte Carlo simulation. In this section we collect the ingredients that arise in the NLO calculation for $g + g \to H$, necessary for the implementation of the POWHEG method.

3.1 Kinematics and phase space

Here we restrict ourselves to considering leading-order processes of the type, $\bar{p}_{\oplus} + \bar{p}_{\ominus} \to \bar{p}_1 + \ldots + \bar{p}_N$, in which all the particles in the N-body final state are either massive or colourless. For such processes the NLO corrections may contain soft singu-

larities and initial-state collinear singularities only. The incoming hadron momenta are labeled $P_\oplus$, for hadrons incident from the $\pm z$ directions, respectively. It therefore follows that the momenta of the colliding, massless partons, with momentum fractions $\bar{x}_\oplus$ and $\bar{x}_\ominus$, are given by $\bar{p}_\oplus = \bar{x}_\oplus P_\oplus$. The momentum of the ith final-state parton produced in the leading-order process is denoted $\bar{p}_i$.

Using $\bar{p}$ to represent the sum of all $\bar{p}_i$, and $\bar{y}$ to signify the rapidity of $\bar{p}$, the phase space for the leading-order process can be written simply as

$$\mathrm{d}\Phi_B \;=\; \mathrm{d}\bar{x}_\oplus \,\mathrm{d}\bar{x}_\ominus \,\mathrm{d}\hat{\Phi}_B \;=\; \frac{1}{s}\,\mathrm{d}\bar{p}^2\,\mathrm{d}\bar{y}\,\mathrm{d}\hat{\Phi}_B, \tag{3.1}$$

where $\mathrm{d}\hat{\Phi}_B$ is the Lorentz invariant phase space for the partonic $2 \to N$ process and s the hadronic centre-of-mass energy. We refer to the variables $\Phi_B = \left\{ \bar{p}^2,\, \bar{y},\, \hat{\Phi}_B \right\}$ as the *Born variables*, where $\hat{\Phi}_B$ parametrizes the N-body phase space in the partonic centre-of-mass frame; for the simple case of a decaying scalar, like the Higgs boson, the matrix element does not depend on $\hat{\Phi}_B$, which could therefore be trivially integrated out at this point.

The NLO real emission corrections to the leading-order process consist of $2 \to N+1$ processes, $p_\oplus + p_\ominus \to p_1 + \ldots + p_N + k$, where we denote the momenta of the same N particles produced in the leading-order process p_i and that of the extra colour charged parton by k. For these processes we introduce the Mandelstam variables $\hat{s}$, $\hat{t}$, $\hat{u}$ and the related *radiative variables* $\Phi_R = \{x,\, y\}$, which parametrize the extra emission:

$$\hat{s} = (p_\oplus + p_\ominus)^2 = \frac{p^2}{x}\,, \tag{3.2a}$$

$$\hat{t} = (p_\oplus - k)^2 \;\; = -\frac{1}{2}\frac{p^2}{x}\,(1-x)\,(1-y)\,, \tag{3.2b}$$

$$\hat{u} = (p_\ominus - k)^2 \;\; = -\frac{1}{2}\frac{p^2}{x}\,(1-x)\,(1+y)\,, \tag{3.2c}$$

where $p = \sum p_i$. We do not explicitly include an azimuthal angle for the gluon about the z axis, instead it is used to define the $+y$ axis relative to which the azimuthal angle of the other final-state particles is measured; ultimately all generated events are randomly rotated about the z axis in the hadronic centre-of-mass frame.

To perform a simultaneous Monte Carlo sampling of the N- and $N+1$-body phase spaces one has to specify the integration variables. We choose two of these to be the mass and rapidity of the system of colourless particles, therefore $\bar{p}^2 \equiv p^2$ and $\bar{y} \equiv y$, where y is the rapidity of p.[2] An immediate consequence of this partial mapping of the N and $N+1$ body phase spaces is that the momentum fractions, $x_\oplus$, of the incident partons in the $2 \to N+1$ processes are related to those of the $2 \to N$ process by

$$x_\oplus = \frac{\bar{x}_\oplus}{\sqrt{x}}\sqrt{\frac{2 - (1-x)\,(1-y)}{2 - (1-x)\,(1+y)}}, \qquad x_\ominus = \frac{\bar{x}_\ominus}{\sqrt{x}}\sqrt{\frac{2 - (1-x)\,(1+y)}{2 - (1-x)\,(1-y)}}, \tag{3.3}$$

where, by definition, $p_\oplus = x_\oplus P_\oplus$.

---

[2]Henceforth we will always refer to these variables as p^2 and y.

Since we restrict ourselves to processes for which the NLO corrections contain at most soft and initial-state collinear singularities, the product of $\hat{t}\,\hat{u}$ with the squared real emission matrix elements will be finite throughout the radiative phase space. Working in conventional dimensional regularization, in $n = 4 - 2\epsilon$ space-time dimensions, we are then able to perform an expansion in ϵ of the $N+1$-body phase-space measure, $\mathrm{d}\Phi_{N+1}$, using similar manipulations to those in refs. [58–61], giving

$$\mathrm{d}\Phi_{N+1} = \mathrm{d}\Phi_B\,\mathrm{d}\Phi_R\,\frac{p^2}{(4\pi)^2\,x^2}\left(\frac{1}{p^2}\right)^\epsilon c_\Gamma\,\mathcal{J}\left(x,y\right), \tag{3.4}$$

where here the Born variables $\hat{\Phi}_B$ specify a configuration in the rest frame of p rather than $\bar{p}$. The function $\mathcal{J}\left(x,y\right)$ is given by

$$\mathcal{J}\left(x,y\right) = \left[\mathcal{S}\,\delta\left(1-x\right) + \mathcal{C}\left(x\right)\left(2\delta\left(1+y\right) + 2\delta\left(1-y\right)\right) + \mathcal{H}\left(x,y\right)\right]\frac{\hat{t}\,\hat{u}}{\hat{s}^2}\,,$$

where

$$\mathcal{S} = \frac{1}{\epsilon^2} - \frac{\pi^2}{6} - \frac{4}{\epsilon}\ln\eta + 8\ln^2\eta\,, \tag{3.5a}$$

$$\mathcal{C}\left(x\right) = -\frac{1}{\epsilon}\frac{1}{\left(1-x\right)_\rho} - \frac{1}{\left(1-x\right)_\rho}\ln x + 2\left(\frac{\ln\left(1-x\right)}{1-x}\right)_\rho\,, \tag{3.5b}$$

$$\mathcal{H}\left(x,y\right) = \frac{2}{\left(1-x\right)_\rho}\left[\left(\frac{1}{1+y}\right)_+ + \left(\frac{1}{1-y}\right)_+\right]\,, \tag{3.5c}$$

with $\rho = \left(\sum_i \sqrt{p_i^2}\right)^2/\hat{s}$ and $\eta = \sqrt{1-\rho}$. The constant c_Γ, which appears due to the use of dimensional regularization, is given by

$$c_\Gamma = (4\pi)^\epsilon\,\frac{\Gamma\left(1-\epsilon\right)^2\Gamma\left(1+\epsilon\right)}{\Gamma\left(1-2\epsilon\right)}\,,$$

and the ρ-distributions are defined by the relation

$$\int_\rho^1 \mathrm{d}x\,h\left(x\right)\left(\frac{\ln^n\left(1-x\right)}{1-x}\right)_\rho = \int_\rho^1 \mathrm{d}x\,\left(h\left(x\right) - h\left(1\right)\right)\frac{\ln^n\left(1-x\right)}{1-x}\,,$$

for any sufficiently regular test function $h\left(x\right)$. The radiative phase space can be parametrized in terms of the radiative variables as

$$\mathrm{d}\Phi_R = \tfrac{1}{2}\mathrm{d}y\,\mathrm{d}x\,. \tag{3.6}$$

The precise definition of $\hat{\Phi}_B$ in the context of the radiative event is, in general, given by a series of boosts and rotations, denoted by $\mathbb{B}$, which *embed* the N-particle, leading-order final state in the $N+1$-particle radiative events. To assemble a radiative event configuration we first construct the N final-state momenta of the leading-order configuration according to the definition of $\hat{\Phi}_B$ and, separately, the momenta of the incident partons and the radiated parton k in the *hadronic* centre-of-mass frame:

$$p_\oplus = \frac{1}{2}\sqrt{s}\left(x_\oplus, 0, 0, +x_\oplus\right)\,, \qquad p = \left(E_T\cosh y, 0, -p_T, E_T\sinh y\right)\,, \tag{3.7}$$

$$p_\ominus = \frac{1}{2}\sqrt{s}\left(x_\ominus, 0, 0, -x_\ominus\right)\,, \qquad k = \left(p_T\cosh y_k, 0, \ p_T, p_T\sinh y_k\right)\,, \tag{3.8}$$

where $E_T = \sqrt{p_T^2 + p^2}$, and

$$p_T^2 = \frac{p^2}{x} \frac{1}{4} \left(1 - y^2\right) \left(1 - x\right)^2 \,, \quad \mathrm{y}_k = \mathrm{y} + \frac{1}{2} \ln\left(\frac{1+y}{1-y}\right) + \frac{1}{2} \ln\left(\frac{2 - (1-x)(1-y)}{2 - (1-x)(1+y)}\right). \tag{3.9}$$

To embed the N final-state particles of the leading-order process in the radiative event we first transform them with a longitudinal boost, $\mathbb{B}_{\mathrm{y}}$, taking us to their rest frame. Should we wish to adhere to the conventions in refs. [58–61], we then apply a rotation to them, $\mathbb{R}$, defined such that, ultimately, $\mathbb{B}$ will preserve the direction of $p_\oplus$, i.e. with $p_\oplus$ defining the $+z$ axis in the p rest frame, and also with the transverse momentum of k defining the y axis. However, for the simple case at hand, no such rotation is necessary since the Higgs boson decays isotropically in its rest frame.[3] A further transverse boost, $\mathbb{B}_T$, parallel with the y axis, is then carried out, where $\mathbb{B}_T^{-1}$ is a transformation from the lab to the frame in which p has no transverse component. Finally, the inverse boost $\mathbb{B}_{\mathrm{y}}^{-1}$ is applied to the N particles, which clearly returns them to a frame where their total rapidity is $\mathrm{y} = \bar{\mathrm{y}}$. Altogether the embedding boost $\mathbb{B}$, to be applied to the leading-order final-state momenta, is given as

$$\mathbb{B} = \mathbb{B}_{\mathrm{y}}^{-1} \, \mathbb{B}_T \, \mathbb{R} \, \mathbb{B}_{\mathrm{y}} \,, \tag{3.10}$$

which, combined with $p_\oplus$, $p_\ominus$ and k in eqs. (3.7), (3.8), completely specifies the radiative kinematics.

3.2 Differential cross section for $a + b \to n$

In this section we restrict ourselves to discussing the general form of the NLO differential cross section for processes of the type $a + b \to i_1 + \ldots + i_N$, where $n = \sum_j i_j$ are colourless particles, which we collectively refer to as *neutrals*. In section 3.3 we give the squared matrix elements for $g + g \to H$ which were ultimately inserted in these formulae. We reiterate that analogous Higgs-strahlung ingredients are *identical* to those in ref. [32] *modulo* the substitution of the $q + \bar{q} \to l + \bar{l}$ leading-order matrix element with that of a given Higgs-strahlung process.

We define the combined incident flux of partons of type a from hadron A, and partons of type b from hadron B, with respective momentum fractions $x_\oplus$ and $x_\ominus$, at a scale μ^2, as

$$\mathcal{L}_{ab}\left(x_\oplus, x_\ominus\right) = f_a^A\left(x_\oplus, \mu^2\right) f_b^B\left(x_\ominus, \mu^2\right) \,, \tag{3.11}$$

where $f_i^I\left(x_i, \mu^2\right)$ are the relevant parton distribution functions (PDFs). To obtain the differential cross section for a real emission process $a + b \to n + c$, we simply multiply the relevant squared matrix element by the phase-space measure in (eq. (3.4)), $\mathcal{L}_{ab}$ and the flux factor $1/2\hat{s}$:

$$\mathrm{d}\sigma_{ab}^{N+1} = \frac{1}{2\hat{s}} \, \mathcal{M}_{ab}^{N+1}\left(p_\oplus, p_\ominus\right) \, \mathcal{L}_{ab}\left(x_\oplus, x_\ominus\right) \, \mathrm{d}\Phi_{N+1}. \tag{3.12}$$

---

[3]As previously noted, the Higgs-strahlung process was simulated in a special way using the Kleiss trick as described in [32].

In general each real emission process makes three contributions to the NLO differential cross section, one for each term in the phase-space measure eq. (3.5): a soft contribution $\mathrm{d}\sigma_{ab}^{S_0}$ proportional to $\delta\left(1-x\right)$, collinear contributions $\mathrm{d}\sigma_{ab}^{C_0\pm}$ proportional to $\delta\left(1\pm y\right)$, and a finite, *hard*, contribution $\mathrm{d}\sigma_{ab}^{H}$ proportional to $\mathcal{H}\left(x,y\right)$. The subscript 0 in $\mathrm{d}\sigma_{ab}^{S_0}$ and $\mathrm{d}\sigma_{ab}^{C_0\oplus}$ reflects the fact that they are bare, divergent, quantities.

For leading-order processes of the type $a+b\to n$ the two initial-state partons must be either a pair of gluons or a quark and an antiquark. The squared matrix elements for the real emission corrections to this process, in which a gluon is emitted from an initial-state parton, $a+b\to n+g$, factorize in the limit that the gluon is soft $(x\to1)$, according to

$$\lim_{x\to1}\mathcal{M}_{ab}^{N+1}\left(p_{\oplus},p_{\ominus}\right)=8\pi\alpha_S\mu^{2\epsilon}\,\frac{1}{p^2}\,2\,C_{ab}\,\frac{\hat{s}^2}{\hat{t}\,\hat{u}}\,\mathcal{M}_{ab}^{N}\left(p_{\oplus},\,p_{\ominus}\right).\qquad(3.13)$$

The colour factor C_{ab} is equal to C_A if a and b are gluons, and C_F if a is a quark and b is an antiquark or *vice versa*. The real emission processes $a+b\to n+g$ are the only ones contributing to the cross section in the limit $x\to1$, all other real emission matrix elements are finite in this limit, hence the product of $\hat{t}\,\hat{u}$ with the squared matrix element vanishes there. Hence, the soft contribution to the NLO differential cross section is

$$\mathrm{d}\sigma_{ab}^{S_0}=\frac{\alpha_S c_\Gamma}{2\pi}\,\left(\frac{\mu^2}{p^2}\right)^\epsilon\,C_{ab}\,\left(\frac{2}{\epsilon^2}-\frac{\pi^2}{3}-\frac{8}{\epsilon}\ln\eta+16\ln^2\eta\right)\,B\left(\Phi_B\right)\,\mathrm{d}\Phi_B,\qquad(3.14)$$

where $B\left(\Phi_B\right)$ is the differential cross section for the leading-order process

$$\mathrm{d}\sigma_{ab}^{B}=B\left(\Phi_B\right)\,\mathrm{d}\Phi_B,\qquad B\left(\Phi_B\right)=\frac{1}{2p^2}\,\mathcal{M}_{ab}^{N}\left(\bar{p}_{\oplus},\,\bar{p}_{\ominus}\right)\mathcal{L}_{ab}\left(\bar{x}_{\oplus},\,\bar{x}_{\ominus}\right).\qquad(3.15)$$

For an arbitrary process in which an initial-state parton a, with momentum $p_{\oplus}$, branches to produce a collinear time-like daughter parton with momentum $k=\left(1-x\right)p_{\oplus}$ and its space-like sister parton $\widetilde{ac}$, with momentum $xp_{\oplus}$, the squared matrix element factorizes according to [62]

$$\lim_{y\to+1}\mathcal{M}_{ab}^{N+1}\left(p_{\oplus},p_{\ominus}\right)=\frac{1}{p^2}\,\frac{\hat{s}^2}{\hat{t}\,\hat{u}}\,8\pi\alpha_S\mu^{2\epsilon}\,\left(1-x\right)\,\hat{P}_{a\,\widetilde{ac}}\left(x\,;\epsilon\right)\,\mathcal{M}_{ab}^{N}\left(xp_{\oplus},p_{\ominus}\right),\qquad(3.16)$$

where we explicitly show the dependence of the N and $N+1$ parton squared matrix elements on the incident parton momenta. Replacing $xp_{\oplus}\leftrightarrow p_{\oplus}$, $a\to b$ in the splitting function we obtain the analogous formula for the case that c is emitted collinear to b $(y\to-1)$. Using this factorization of the matrix element, the collinear contributions to the real emission cross section, arising from initial-state radiation, are seen to have the general form,

$$\begin{aligned}
\mathrm{d}\sigma_{ab}^{C_0\oplus}&=\mathrm{d}\sigma_{ab}^{SC\oplus}+\mathrm{d}\sigma_{ab}^{C\oplus}-\mathrm{d}\sigma_{ab}^{CT\oplus},\\
\mathrm{d}\sigma_{ab}^{SC\oplus}&=\frac{\alpha_S c_\Gamma}{2\pi}\,\left(\frac{\mu^2}{p^2}\right)^\epsilon\,C_{i\,\widetilde{ic}}\left(p_{i\,\widetilde{ic}}+4\ln\eta\right)\left(\frac{1}{\epsilon}+\ln\left(\frac{p^2}{\mu^2}\right)\right)\,B\left(\Phi_B\right)\,\mathrm{d}\Phi_B,\\
\mathrm{d}\sigma_{ab}^{C\oplus}&=\frac{\alpha_S}{2\pi}\,\mathcal{C}_{i\,\widetilde{ic}}^{\oplus}\left(x\right)\,B^{\oplus}\left(\Phi_B\right)\,\widehat{\mathcal{L}}_{ab}^{\oplus}\left(x_{\oplus},\,x_{\ominus}\right)\,\frac{1}{x}\,\mathrm{d}\Phi_B\,\mathrm{d}x,\\
\mathcal{C}_{i\,\widetilde{ic}}^{\oplus}\left(x\right)&=\left[\frac{1}{\left(1-x\right)_\rho}\ln\left(\frac{p^2}{\mu^2 x}\right)+2\left(\frac{\ln\left(1-x\right)}{1-x}\right)_\rho\right]\left(1-x\right)\hat{P}_{i\,\widetilde{ic}}\left(x\right)-\hat{P}_{i\,\widetilde{ic}}^{\epsilon}\left(x\right),\\
\mathrm{d}\sigma_{ab}^{CT\oplus}&=\frac{1}{\epsilon}\,\frac{\alpha_S}{2\pi}\,P_{i\,\widetilde{ic}}\left(x\right)\,B^{\oplus}\left(\Phi_B\right)\,\widehat{\mathcal{L}}_{ab}^{\oplus}\left(x_{\oplus},\,x_{\ominus}\right)\,\frac{1}{x}\,\mathrm{d}\Phi_B\,\mathrm{d}x,
\end{aligned}\qquad(3.17)$$

– 9 –

where $i = a$ in the case that parton a splits to produce parton c, and $i = b$ for the case that parton b branches to produce c. $\hat{P}_{i\,\widetilde{i}c}(x; \epsilon)$ and $P_{i\,\widetilde{i}c}(x)$ are the bare and regularized Altarelli-Parisi kernels given in appendix A; $C_{i\,\widetilde{i}c}\, p_{i\,\widetilde{i}c}$ is equal to the coefficient of the $\delta(1-x)$ term in the latter, for the case $\rho = 0$. The $B^{\oplus}$ and $\widehat{\mathcal{L}}^{\oplus}$ functions are related to the leading-order differential cross section and parton flux:

$$B^{\oplus}(\Phi_B) = \frac{1}{2p^2}\, \mathcal{M}_{ab}^N(xp_{\oplus}, p_{\ominus})\, \mathcal{L}_{ab}(\bar{x}_{\oplus}, \bar{x}_{\ominus})\,, \qquad \widehat{\mathcal{L}}_{ab}^{\oplus}(x_{\oplus}, x_{\ominus}) = \frac{\mathcal{L}_{ab}\left(\frac{\bar{x}_{\oplus}}{x}, \bar{x}_{\ominus}\right)}{\mathcal{L}_{ab}(\bar{x}_{\oplus}, \bar{x}_{\ominus})}\,,$$
$$B^{\ominus}(\Phi_B) = \frac{1}{2p^2}\, \mathcal{M}_{ab}^N(p_{\oplus}, xp_{\ominus})\, \mathcal{L}_{ab}(\bar{x}_{\oplus}, \bar{x}_{\ominus})\,, \qquad \widehat{\mathcal{L}}_{ab}^{\ominus}(x_{\oplus}, x_{\ominus}) = \frac{\mathcal{L}_{ab}\left(\bar{x}_{\oplus}, \frac{\bar{x}_{\ominus}}{x}\right)}{\mathcal{L}_{ab}(\bar{x}_{\oplus}, \bar{x}_{\ominus})}\,.$$

$$(3.18)$$

In the $\overline{\text{MS}}$ scheme each collinear singular $\mathrm{d}\sigma_{ab}^{CT\,\oplus}$ term in the cross section is exactly compensated for by an additive collinear counter term identical to it (hence the CT labeling). This amounts to absorbing the divergence in the PDFs, renormalizing them, hence we now omit them. The only remaining divergences are soft and collinear terms $\mathrm{d}\sigma_{ab}^{SC\,\oplus}$, which we absorb in the soft contribution to the cross section $\mathrm{d}\sigma_{ab}^{S_0}$.

Absorbing the soft and collinear terms $\mathrm{d}\sigma_{ab}^{SC\,\oplus}$ in the soft contribution to the cross section eq. (3.14), redefines it as

$$\mathrm{d}\sigma_{ab}^{S_0} = \mathcal{S}_0\, B(\Phi_B)\, \mathrm{d}\Phi_B\,, \tag{3.19}$$

where

$$\mathcal{S}_0 = \frac{\alpha_S c_\Gamma}{2\pi}\left(\frac{\mu^2}{p^2}\right)^\epsilon C_{ab}\left[\frac{2}{\epsilon^2} + \frac{2}{\epsilon}\, p_{a\,\widetilde{a}g} + \ln\left(\frac{p^2}{\mu^2}\right)\left(2p_{a\,\widetilde{a}g} + 8\ln\eta\right) + 16\ln^2\eta - \frac{\pi^2}{3}\right]. \tag{3.20}$$

One must consider also the contribution of virtual corrections to the leading-order process as well as the real corrections above. Again, for $a + b \to n$ processes, these have a simple form (see e.g. ref. [29])

$$\lim_{x\to 1} \mathcal{M}_{ab}^{N\,V}(\bar{p}_{\oplus}, \bar{p}_{\ominus}) = \mathcal{V}_0\, \mathcal{M}_{ab}^N(\bar{p}_{\oplus}, \bar{p}_{\ominus}) \tag{3.21}$$

with

$$\mathcal{V}_0 = \frac{\alpha_S c_\Gamma}{2\pi}\left(\frac{\mu^2}{p^2}\right)^\epsilon C_{ab}\left[-\frac{2}{\epsilon^2} - \frac{2}{\epsilon}\, p_{a\,\widetilde{a}g} - \frac{\pi^2}{3}\right] + \widehat{\mathcal{M}}_{ab}^{N\,V_{\text{reg}}}(\bar{p}_{\oplus}, \bar{p}_{\ominus})\,, \tag{3.22}$$

where $\widehat{\mathcal{M}}_{ab}^{N\,V_{\text{reg}}}$ is the remainder of the virtual correction, regular as $\epsilon \to 0$, divided by the leading-order squared matrix element,

$$\widehat{\mathcal{M}}_{ab}^{N\,V_{\text{reg}}}(\bar{p}_{\oplus}, \bar{p}_{\ominus}) = \frac{\mathcal{M}_{ab}^{N\,V_{\text{reg}}}(\bar{p}_{\oplus}, \bar{p}_{\ominus})}{\mathcal{M}_{ab}^N(\bar{p}_{\oplus}, \bar{p}_{\ominus})}\,. \tag{3.23}$$

The poles in ϵ in $\mathcal{V}_0$ will exactly cancel those in $\mathcal{S}_0$ making the differential cross section finite for $\epsilon \to 0$.

The cross section for the $a + b \to n$ leading-order process, combined with the virtual corrections and $a + b \to n + g$ real emission corrections, may then be written as

$$\mathrm{d}\sigma_{ab} = B(\Phi_B)\, \mathrm{d}\Phi_B + V(\Phi_B)\, \mathrm{d}\Phi_B + R_{ab}(\Phi_B, \Phi_R)\, \mathrm{d}\Phi_B\, \mathrm{d}\Phi_R, \tag{3.24}$$

where $V(\Phi_B)$ results from the combination of the soft and virtual corrections to the cross section (eqs. (3.19), (3.20)),

$$V(\Phi_B) = \mathcal{V} B(\Phi_B) , \qquad\qquad \mathcal{V} = \mathcal{S}_0 + \mathcal{V}_0|_{\epsilon=0} , \qquad\qquad (3.25)$$

and $R(\Phi_B, \Phi_R)$ results from the remaining collinear and hard real emission corrections,

$$R_{ab}(\Phi_B, \Phi_R) = \frac{\alpha_S}{2\pi} \frac{1}{x} \mathcal{R}_{ab} \widehat{\mathcal{L}}_{ab}(x_\oplus, x_\ominus) B(\Phi_B) ,$$

$$\mathcal{R}_{ab} = 2\mathcal{C}^\oplus_{a\,\widetilde{a}c}(x) \delta(1-y) + 2\mathcal{C}^\ominus_{b\,\widetilde{b}c}(x) \delta(1+y) + \mathcal{H}_{ab} , \qquad (3.26)$$

$$\mathcal{H}_{ab} = \frac{x\,\hat{t}\,\hat{u}}{\hat{s}} \frac{1}{8\pi\alpha_S} \frac{\mathcal{M}^{N+1}_{ab}(p_\oplus, p_\ominus)}{\mathcal{M}^N_{ab}(\bar{p}_\oplus, \bar{p}_\ominus)} \mathcal{H}(x,y) .$$

Note that in writing eq. (3.24) we have tacitly equated $\mathcal{M}^N(xp_\oplus, p_\ominus) = \mathcal{M}^N(p_\oplus, xp_\ominus) = \mathcal{M}^N(\bar{p}_\oplus, \bar{p}_\ominus)$ in the collinear term. This is possible due to our defining $p^2 = \bar{p}^2$ and $y = \bar{y}$ in section. 3.1.

The remaining contributions to the full NLO differential cross section are due to the production of n via new channels. For $q + \bar{q} \to n$ processes we add contributions arising from the $q + g \to n + q$ channel,

$$R_{qg}(\Phi_B, \Phi_R) = \frac{\alpha_S}{2\pi} \frac{1}{x} \mathcal{R}_{qg} \widehat{\mathcal{L}}_{qg}(x_\oplus, x_\ominus) B(\Phi_B) , \qquad (3.27)$$

$$\mathcal{R}_{qg} = 2\mathcal{C}_{gq}\delta(1+y) + \mathcal{H}_{qg} ,$$

$$\mathcal{H}_{qg} = \frac{x\,\hat{t}\,\hat{u}}{\hat{s}} \frac{1}{8\pi\alpha_S} \frac{\mathcal{M}^{N+1}_{qg}(p_\oplus, p_\ominus)}{\mathcal{M}^N_{ab}(\bar{p}_\oplus, \bar{p}_\ominus)} \mathcal{H}(x,y) ,$$

and also a set of terms due to the $\bar{q} + g \to n + \bar{q}$ channel, identical up to the replacement $q \to \bar{q}$ on all terms with the exception of $\mathcal{C}_{gq}$. For the $g + g \to n$ process we add a contribution from $g + q \to n + q$, for which R_{gq} has the same form as eq. (3.27), *modulo* interchanging the subscripts $qg \leftrightarrow gq$, and a further contribution from the $g + \bar{q} \to n + \bar{q}$ process, derived from the former by replacing $q \to \bar{q}$ on all terms but $\mathcal{C}_{qg}$.

3.3 $g + g \to H$ matrix elements

The squared, spin and colour averaged, leading-order matrix element for the $g + g \to H$ process is given by

$$\mathcal{M}^N_{gg}(\bar{p}_\oplus, \bar{p}_\ominus) = \mathcal{M}^N_{gg} = \frac{\mathcal{N} p^4}{576\pi(1-\epsilon)} , \qquad (3.28)$$

where $\mathcal{N} = \frac{\alpha_S^2 \mu^{2\epsilon}}{\pi v^2}$, with v the vacuum expectation value of the Higgs field and the scale μ emerging from the use of conventional dimensional regularization. The real emission radiative corrections consist of three processes: $g + g \to H + g$; $q + g \to H + q$; and $q + \bar{q} \to H + g$. As noted above, the singular, soft and/or collinear, limits of the matrix elements, associated to the ϵ poles in $d\Phi_{N+1}$, are universal, therefore a full calculation of the matrix elements is only needed to multiply the $\mathcal{H}(x,y)$ term in $d\Phi_{N+1}$. Since the term

proportional to $\mathcal{H}(x, y)$ contains no poles in ϵ, the full calculation of the squared matrix elements can be carried out in four dimensions, giving,

$$\mathcal{M}_{gg}^{N+1} = 8\pi\alpha_S \, \mathcal{M}_{gg}^N \, \frac{3}{p^4} \, \frac{1}{\hat{s}\hat{t}\hat{u}} \, \left[p^8 + \hat{s}^4 + \hat{t}^4 + \hat{u}^4\right] \,, \quad \mathcal{M}_{gq}^{N+1} = 8\pi\alpha_S \, \mathcal{M}_{gg}^N \, \frac{-4}{3p^4} \, \frac{1}{\hat{u}} \, \left[\hat{s}^2 + \hat{t}^2\right] \,,$$
(3.29)

$$\mathcal{M}_{q\bar{q}}^{N+1} = 8\pi\alpha_S \, \mathcal{M}_{gg}^N \, \frac{32}{9p^4} \, \frac{1}{\hat{s}} \, \left[\hat{u}^2 + \hat{t}^2\right] \,, \qquad\qquad \mathcal{M}_{g\bar{q}}^{N+1} = \mathcal{M}_{gq}^{N+1} \,.$$

The squared matrix element $\mathcal{M}_{qg}^{N+1}$ can be obtained from $\mathcal{M}_{gq}^{N+1}$ by crossing symmetry simply by interchanging $\hat{u} \leftrightarrow \hat{t}$.

The $\mathcal{O}(\alpha_S)$ virtual corrections to the $g + g \rightarrow H$ process consist of purely gluonic swordfish and triangle vertex corrections, as well as a UV counter term. At NLO these corrections contribute to the cross section through their interference with the leading-order amplitude, their form is precisely that in eq. (3.22) with,

$$\mathcal{M}_{gg}^{V\,\mathrm{reg}} = \frac{\alpha_S}{2\pi} \, C_A \left[\frac{11}{3} + \frac{4}{3}\pi^2 - \frac{4\pi b_0}{C_A} \ln\left(\frac{p^2}{\mu_R^2}\right)\right] \mathcal{M}_{gg}^B \,,$$
(3.30)

where μ_R is the renormalization scale. When used with the general expressions in section 3.2, these are all the ingredients required to write down the $\overline{B}(\Phi_B)$ function and the modified Sudakov form factors for this process (eqs. (2.2), (2.3)).

4 Implementation

4.1 Generation of the leading-order configuration

The first phase of the simulation involves generating a leading-order configuration by sampling the $\overline{B}(\Phi_B)$ function (see section 2, eq. (2.2)), which is the NLO differential cross section integrated over the radiative variables,

$$\overline{B}(\Phi_B) = B(\Phi_B) \left[1 + \mathcal{V} + \sum_{ab} \int d\Phi_R \, \frac{\alpha_S}{2\pi} \, \frac{1}{x} \, \mathcal{R}_{ab} \, \widehat{\mathcal{L}}_{ab}(x_\oplus, x_\ominus)\right] \,.$$
(4.1)

Here the summation runs over all real emission processes $a + b \rightarrow n + c$ contributing at NLO. Since the leading-order process is factorized inside the real emission terms R_{ab}, the $\overline{B}(\Phi_B)$ distribution can be generated efficiently by just reweighting the leading-order cross section.

The dependency of the x integration limits on the y radiative variable, coupled with the definitions of the ρ and plus distributions, is a significant obstacle to the numerical implementation. We may obtain fixed integration limits by a simple change of variables $x \rightarrow \tilde{x}$, where $\tilde{x}$ is defined through the relation

$$x(\tilde{x}, y) = \bar{x}(y) + \bar{\eta}(y)^2 \, \tilde{x} \,, \qquad\qquad \bar{\eta}(y) = \sqrt{1 - \bar{x}(y)}.$$
(4.2)

Care must be taken in implementing these changes of variables in the NLO differential cross section, particularly with regard to the plus and ρ distributions. When the transformation is complete only plus distributions remain since, unlike x, $\tilde{x}$ extends over the range $[0, 1]$ for

all y. Numerical implementation of the $\overline{B}\left(\Phi_B\right)$ distribution requires all plus distributions be replaced by regular functions; due to the change of variables in eq. (4.2) this is now trivial since all plus distributions are to be integrated over exactly the domains specified in their definition $0 \le \tilde{x} \le 1$.

After the change of variables, the generation of the N-body configurations is technically carried out in the same way as in ref. [32]: N-body configurations are first generated using the corresponding leading-order Herwig++ simulation, after which they are reweighted and retained with a probability proportional to the integrand of eq. (4.1), which is sampled using a VEGAS based algorithm [63].

4.2 Generation of the hardest emission

Given an N-body configuration generated according to $\overline{B}\left(\Phi_B\right)$, we proceed to generate the largest transverse momentum emission according to the modified Sudakov form factor in eq. (2.3). The exponent in the modified Sudakov form factor consists of an integral over a sum of different contributions, one for each channel, $a + b \to n + c$, given by

$$W_{ab}\left(\Phi_R, \Phi_B\right) = \frac{\widehat{R}_{ab}\left(\Phi_B, \Phi_R\right)}{B\left(\Phi_B\right)} = \frac{\alpha_S}{2\pi}\frac{1}{x}\widehat{\mathcal{H}}_{ab}\,\widehat{\mathcal{L}}_{ab}\left(x_\oplus, x_\ominus\right)\,, \tag{4.3}$$

where $\widehat{\mathcal{H}}_{ab}$ is equal to $\mathcal{H}_{ab}$ with the plus and ρ regularization prescriptions omitted.

Instead of generating the hardest emission in terms of $\Phi_R = \{x, y\}$ we find it more convenient to make a change of variables to $\Phi_R' = \{p_T, \mathrm{y}_k\}$, defined in eq. (3.9). Making this change of variables removes the complicated θ-function in eq. (2.3), replacing it by a lower bound on the integration over p_T:

$$\Delta_{\hat{R}}\left(p_T\right) = \exp\left(-\int_{p_T}^{p_{T\mathrm{max}}} \mathrm{d}\Phi_R \sum_{ab} W_{ab}\left(\Phi_R, \Phi_B\right)\right)\,, \tag{4.4}$$

where the upper bound, $p_{T_{\max}}$, is due to the usual basic phase-space considerations. The distribution of the transformed radiative variables arising from $\Delta_{\hat{R}}\left(p_T\right)$ (eq. (2.3)) is sampled using a *veto algorithm* [64], in precisely the same way as was done in ref. [32]. If an emission is generated it is reconstructed from the p_T and y_k radiative variables according to eqs. (3.7), (3.8).

When generating the hardest emission we use a factorization scale of the transverse mass of the Higgs boson or off-shell vector boson, in gluon fusion and Higgs-strahlung processes, respectively. In both cases we use the p_T of the boson as renormalization scale. This is required to correctly treat the small p_T region where the POWHEG results should agree with the default Herwig++ parton shower.

4.3 Truncated and vetoed parton showers

The Herwig++ shower algorithm [44, 65] works by evolving downward in a variable related to the angular separation of parton branching products, $\tilde{q}$, starting at a scale determined by the colour flow and kinematics of the underlying hard scattering process, and ending at an infrared cut-off, beneath which further emissions are defined to be *unresolvable*. Each

branching is specified by an evolution scale $\tilde{q}$, a light-cone momentum fraction, z, and an azimuthal angle, ϕ. The momenta of all particles forming a shower can be uniquely constructed given the $\{\tilde{q},\, z,\, \phi\}$ parameters of each branching. Since the showers from each parton in a given process evolve independently, from what are initially on-shell particles, generated according to a matrix element, some reshuffling of these momenta, after the generation of the parton showers, is required to ensure global energy-momentum conservation.

In order to carry out showering of $N{+}1$-body final states associated to the generation of the hardest emission, we treat the $N{+}1$ momenta as having arisen from the showering of an N-body configuration with the Herwig++ shower. To this end we calculate the branching parameters $\{\tilde{q}_h,\, z_h,\, \phi_h\}$ for which the shower would reconstruct the $N{+}1$-body system from an initial N-body one. Details of this *inverse reshuffling* calculation were given already in [32]. The POWHEG emission is subsequently regenerated in the course of a single Herwig++ shower as follows:

1. the shower evolves from the default starting scale to $\tilde{q}_h$, with the imposition that any further emissions be flavour conserving and of lower p_T than that of the hardest emission (p_{T_h}), the *truncated shower*;

2. the hardest emission is inserted as a set of branching parameters $\{\tilde{q}_h,\, z_h,\, \phi_h\}$;

3. the evolution continues down to the cut-off scale, vetoing any emissions whose transverse momentum exceeds p_{T_h}, the *vetoed shower*.

Should the hardest emission occur in an area of phase space that the shower cannot populate, i.e. the wide angle/high p_T *dead zone* (section 5.2.1), subsequent emissions will have sufficient resolving power to *see* the widely separated emitters individually. It follows that no truncated shower is then required, since this models coherent, large angle emission from more collimated configurations of partons, and so we proceed directly to the vetoed shower.

5 Results

In this section we present predictions from our POWHEG simulations of the $g + g \to H$ and $q + \bar{q} \to V + H$ processes within the Herwig++ event generator. By comparing our results to other predictions, based on independent calculations and methods, we aim to validate these realisations of the formalism.

In section 5.1 we seek to check the calculation and implementation of the POWHEG NLO differential cross section and $\overline{B}\,(\Phi_B)$ functions, eqs. (2.1)-(2.2), we thereby check the NLO accuracy of the calculation and in particular the generation of the Born variables (section 4.1). Technically this is the most delicate part of the simulation, requiring a full calculation and numerical implementation of the NLO differential cross section. We compare our results to the NLO parton level Monte Carlo program MCFM [47] to this end.

In section 5.2 we move to focus on distributions sensitive to the generation of the hardest emission (section 4.2) and the subsequent merging with the shower algorithm. Here we compare our results to three different approaches: the bare angular-ordered parton shower, the parton shower including *matrix element corrections* and also MC@NLO. While

MC@NLO consistently combines NLO calculations with the HERWIG parton shower, matrix element corrections work to adjust the distribution of the hardest emission from the Herwig++ parton shower to be equal to that of the *real part* of the NLO contribution. Matrix element corrections also serve to populate an area of the real emission phase space which the shower cannot ordinarily reach, the so-called *dead-zone*, which we describe fully in section 5.2. Since the effects of the NLO contributions on the normalisation of the results are examined in detail in section 5.1 and, moreover, the predictions from the shower, with and without matrix element corrections, have leading-order normalisations, in section 5.2 we concentrate on the shapes of these distributions.

Note that we use the notation $\mathcal{O}(\alpha_S^n)$ to denote terms of order α_S^n *relative* to the leading order contribution.

5.1 POWHEG differential cross sections and $\overline{B}(\Phi_B)$

In order to check the calculation of the POWHEG differential cross section and $\overline{B}(\Phi_B)$ functions, eqs. (2.1)-(2.2), total cross sections and differential distributions were compared between our POWHEG implementation and the parton level NLO program MCFM [47]. Since MCFM computes the effects of fixed order (NLO) corrections to the processes in question, these comparisons are performed prior to any showering of the POWHEG NLO configurations by Herwig++.

In carrying out these comparisons both Herwig++ and MCFM were run using the MRST2001 NLO [66] parton distribution set via the LHAPDF interface [67]. A fixed, constant, factorization and renormalization scale of 100 GeV was used, in order to eliminate small variations in the treatment of the running coupling and PDF evolution as a possible source of discrepancy. Also, for this part of the validation, we have assumed the Higgs boson mass to be 115 GeV. In all cases the total cross sections from MCFM and our POWHEG implementation agreed to within 0.5 %.

The gluon fusion process is rather simple in view of the fact that the scalar Higgs boson decays isotropically in its rest frame. Consequently the only non-trivial distributions to check are the mass and rapidity of the Higgs boson. These distributions are plotted for the process[4] $gg \to H \to \tau^+\tau^-$ in figure 1 and everywhere exhibit a high level of agreement with MCFM.

The Higgs-strahlung process is more involved than the gluon fusion process due to the intermediate particle having spin-1 and due to our re-using the method in our earlier POWHEG work, employing the Kleiss trick [45, 46] to generate the NLO corrections independently of the details of the decay of the initially off-shell vector boson. Therefore, to check the correctness of this method, one must look closely at the distributions of the final-state particles, particularly, on account of propagating spin correlation effects, the vector boson and its decay products.

The variety of Higgs-strahlung processes which can be simulated by MCFM is limited, unlike Herwig++, hence we opted to carry out the Higgs-strahlung comparisons using the following processes: $q\bar{q} \to HW^+ \to e^+\nu_e b\bar{b}$, $q\bar{q} \to HW^- \to e^-\bar{\nu}_e b\bar{b}$, $q\bar{q} \to HZ \to e^+e^-b\bar{b}$.

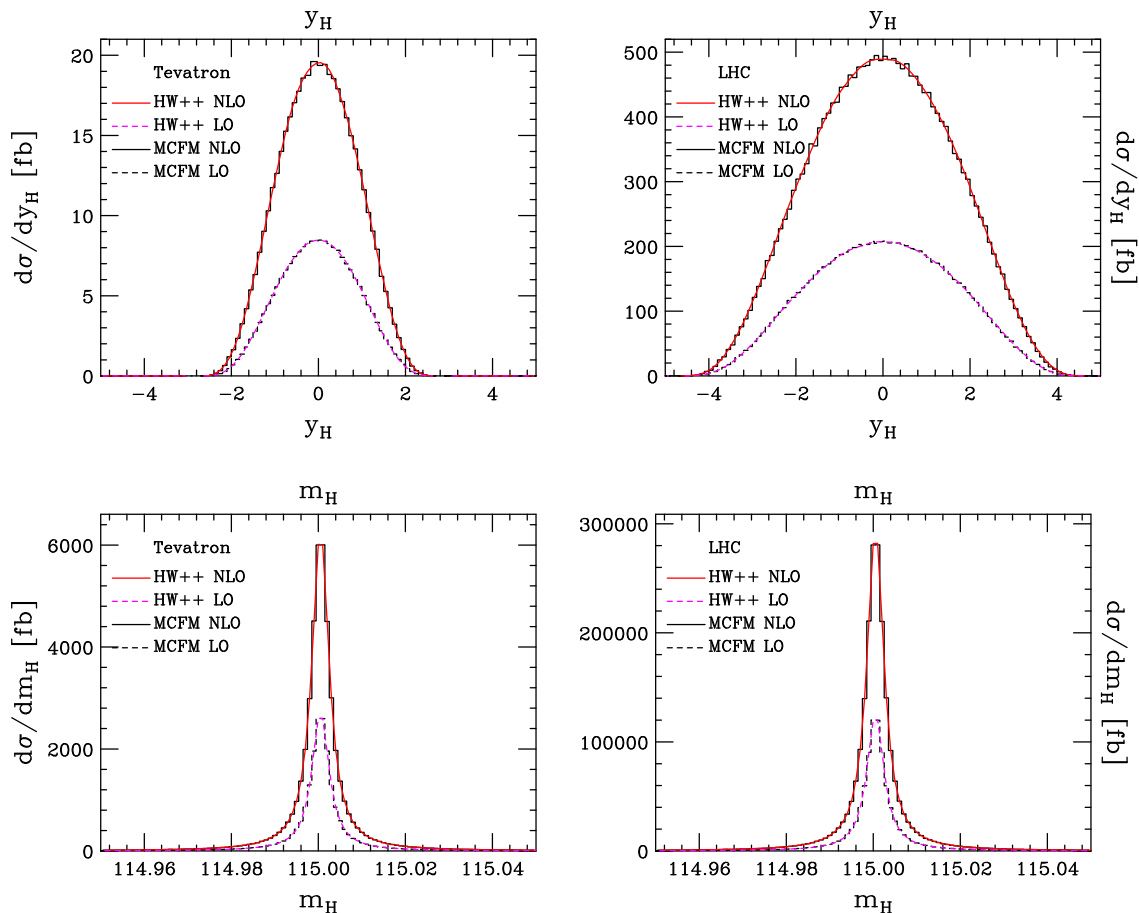[4]MCFM does not implement the $gg \to H \to \gamma\gamma$ process.

Figure 1. Comparisons of the POWHEG implementation in Herwig++ and the NLO parton level code MCFM [47], for the Higgs boson rapidity (y_H) and mass (m_H) distributions in the process $g\,g \to H \to \tau^+\tau^-$. Results on the left are obtained for $p\bar{p}$ collisions at the Tevatron ($\sqrt{s} = 1.96\,\text{TeV}$) while those on the right are for LHC pp collisions ($\sqrt{s} = 14\,\text{TeV}$).

In figure 2 we show the mass of the initial off-shell vector boson, one of the Born variables for this process, for which there is very good agreement between our POWHEG result and that of MCFM. In figures 2–6, we show a number of distributions with sensitivity to the details of the decay of the vector boson, specifically, the polar angle of the lepton produced by the decaying, resonant, vector boson in its rest frame, the pseudorapidity of the final-state lepton, as well as the rapidity and transverse momentum of the resonant vector boson decaying to leptons. In all cases the agreement between our code and MCFM is very good.

5.2 Hardest emission generation and showering

In this section we focus on the distributions most sensitive to the generation of the hardest emission (section 4.2) and any further radiation obtained due to merging with the shower algorithm (sections 2, 4.3). In particular we study the p_T spectra of the Higgs boson in the gluon fusion process and the colourless vector boson plus Higgs boson system in
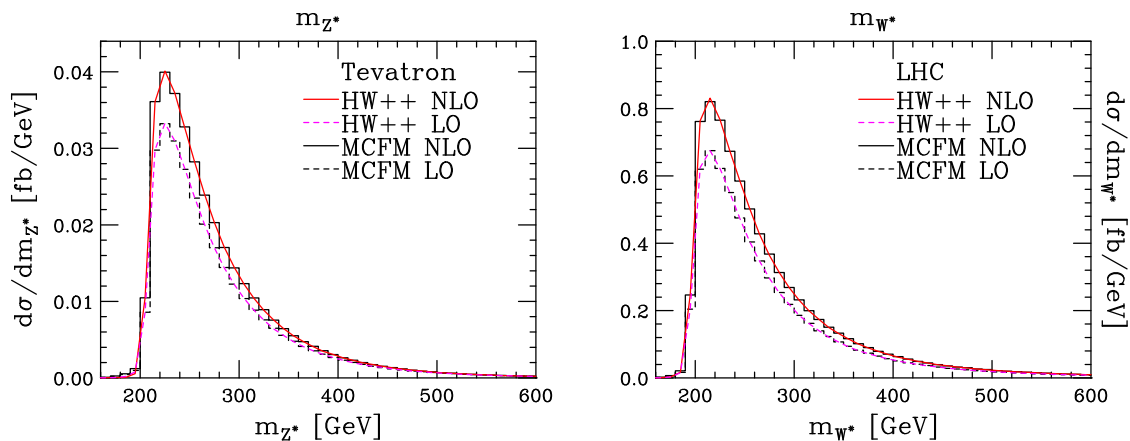
Figure 2. Mass of the off-shell virtual vector boson in $q\bar{q} \rightarrow HZ$ and $q\bar{q} \rightarrow HW^-$ processes, in the left and right-hand plots respectively. The $q\bar{q} \rightarrow HZ$ predictions are for $1960\,\mathrm{GeV}$, Tevatron, proton-antiproton collisions, while the $q\bar{q} \rightarrow HW^-$ predictions are for $14\,\mathrm{TeV}$, LHC, proton-proton collisions. This mass is one of the so-called *Born variables* in the NLO differential cross section (see section 3.1 and ref. [32]).

Higgs-strahlung processes. The distributions of the rapidity difference between the leading, highest p_T, jet and the produced colour neutral systems, $y_{\mathrm{jet}} - y_{\mathrm{H}}$ and $y_{\mathrm{jet}} - y_{\mathrm{VH}}$, are given special attention, particularly in view of the differences noted in previous works on the POWHEG formalism, arising between it and MC@NLO [28, 33, 41].

Since we generate the hardest emission directly in terms of p_T it is clear that the p_T spectra are a direct test of this part of the work. The relevance of the $y_{\mathrm{jet}} - y_{\mathrm{H}}$ and $y_{\mathrm{jet}} - y_{\mathrm{VH}}$ distributions to these investigations is not immediately obvious. However, the $y_{\mathrm{jet}} - y_{\mathrm{H}}$ and $y_{\mathrm{jet}} - y_{\mathrm{VH}}$ variables, for one emission, can be expressed *purely* in terms of the radiative variables x and y, they are in fact both equal to $y_k - y$ as given by eq. (3.9), hence they are also an ideal probe of the hardest emission generation. In order to gain some physical insight into what this variable really means, we note that in the limit that the angle between the radiated parton and colliding beam partons tends to 90°, in the partonic centre-of-mass frame, eq. (3.9) approximates to

$$y_k - y = -\frac{2}{1+x}\left(\theta - \frac{\pi}{2}\right),\tag{5.1}$$

where we remind the reader that θ is the angle between the emitted parton and the $p_\oplus$ parton in that frame. Furthermore, from eq. (3.9) one can see that $y_k - y$ is maximised when the radiated parton is anticollinear to $p_\oplus$ and minimised when it is collinear to $p_\oplus$. Put simply, the central region of the $y_k - y$ distribution is populated by wide angle radiation while the tails are due to collinear radiation.

The jets are defined using the longitutinal invariant k_T algorithm [68] with an angular measure $\Delta R = \sqrt{\Delta\eta^2 + \Delta\phi^2}$, where $\Delta\eta$ and $\Delta\phi$ are the pseudorapidity and azimuthal angle differences between two particles respectively, and the E recomination scheme, as implemented in the KtJet package [69].
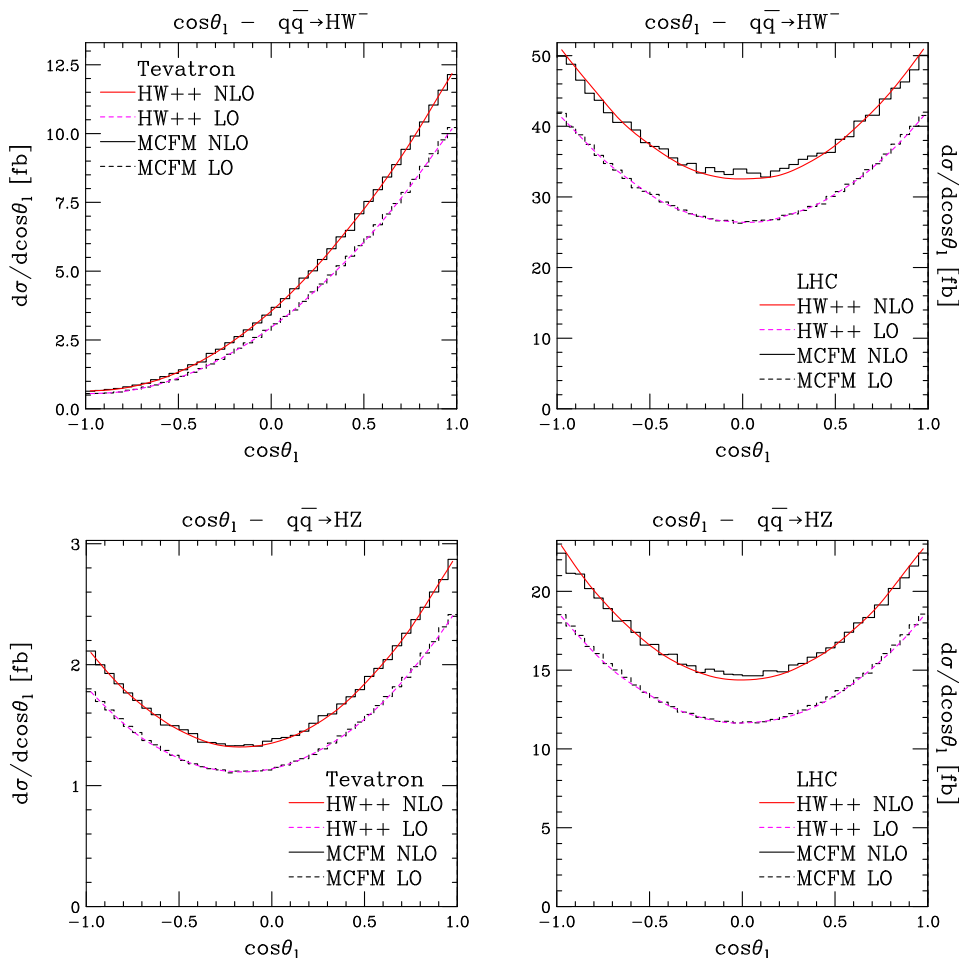
Figure 3. The polar angle of the electron produced by the vector boson, in its rest frame, in Higgs-strahlung processes. The uppermost plots concern the $q\bar{q} \rightarrow HW^-$ process and the lower plots relate to the $q\bar{q} \rightarrow HZ$ process. For each process we have displayed the results obtained at the Tevatron on the left and the LHC on the right. The leading-order (LO) predictions of Herwig++ and MCFM [47] are shown as dashed lines while solid lines represent the corresponding NLO predictions. This is a very important test of the correctness of the Kleiss trick, which we have used to generate the NLO corrections independently of the generation of the LO process [32].

In studying the Higgs-strahlung process we shall compare our results to three different approaches, namely, the bare angular-ordered parton shower in Herwig++, the Herwig++ parton shower including matrix element corrections and also MC@NLO. In the case of the gluon fusion process we compare to a further fourth prediction which is given by modifying the hard component of the matrix element corrections in Herwig++.

5.2.1 The dead zone

In order to better understand the predictions from the Herwig++ shower, with and without matrix element corrections, and also those of MC@NLO, it will help to understand the phase space available for the first emission in the shower approach.
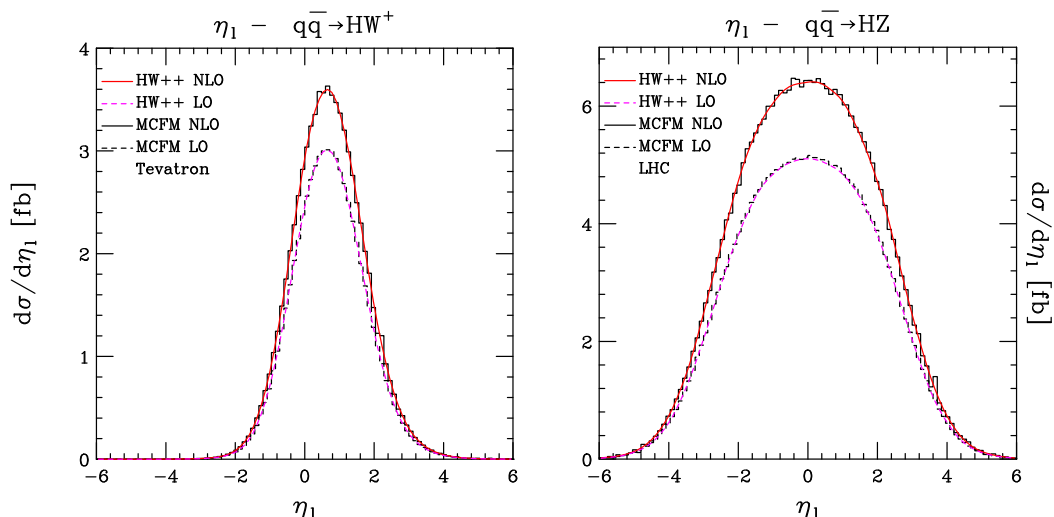
Figure 4. The pseudorapidity of the electron produced by the decaying vector boson, in $q\bar{q} \to HW^+$ (left) and $q\bar{q} \to HZ$ (right) Higgs-strahlung processes, from the POWHEG implementation and also MCFM. As in figure 3 the predictions for the Tevatron are given on the left ($p\bar{p}$, $\sqrt{s} = 1.96\,\text{TeV}$) and for the LHC on the right (pp, $\sqrt{s} = 14\,\text{TeV}$). As well as the distribution of the lepton polar angle, this is a critical test of the implementation of the Kleiss trick which factorizes the generation of the LO and NLO calculations [32]. It shows that all spin correlations have been correctly propagated through to the vector boson decay products.
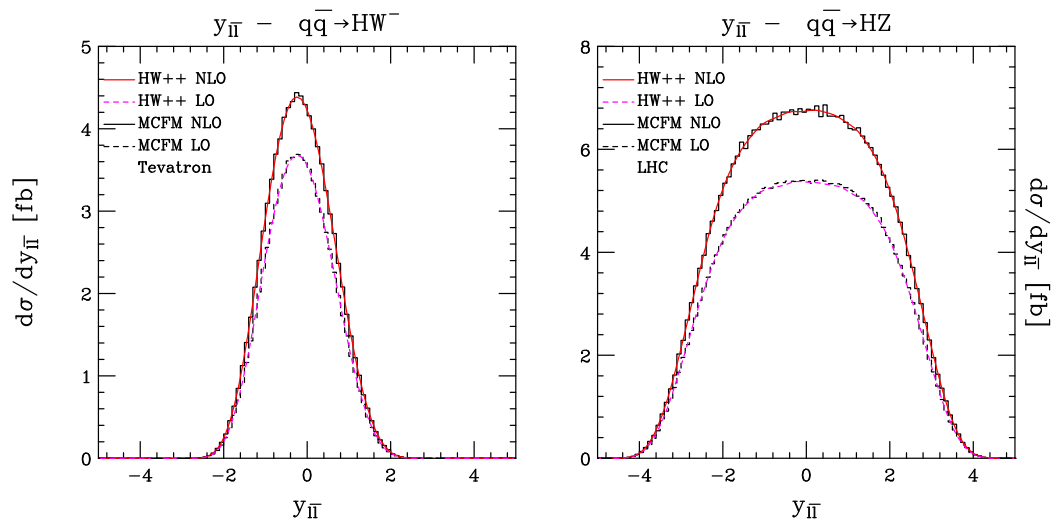
Figure 5. The rapidity distributions of the resonant vector boson in the Higgs-strahlung processes, obtained with MCFM and the Herwig++ POWHEG implementation. The left-hand plot was obtained considering the $q\bar{q} \to HW^-$ process while the right-hand plot relates to the $q\bar{q} \to HZ$ process. As with the previous figures, on the left-hand side we show predictions for the Tevatron and, on the right, predictions for the LHC. This is another fundamental test of the functioning of the Kleiss trick, since, in using this trick, the generation of the radiative variables is *completely* independent of the generation of the decay of the *virtual vector boson viz.* the Higgs boson and the resonant vector boson.
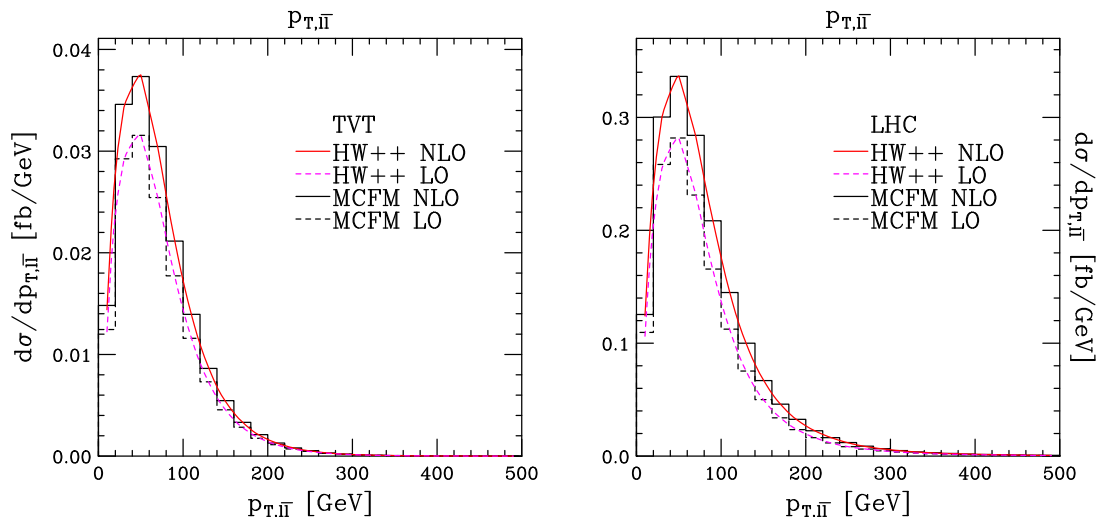
Figure 6. The transverse momentum of the Z boson in Higgs-strahlung events at the Tevatron, compared to MCFM. On the right hand side we show an analogous comparison for the LHC. This distribution is a further confirmation that the Kleiss trick is working correctly, since it is sensitive to the details of the final state and not simply the production of the initial off-shell vector boson.
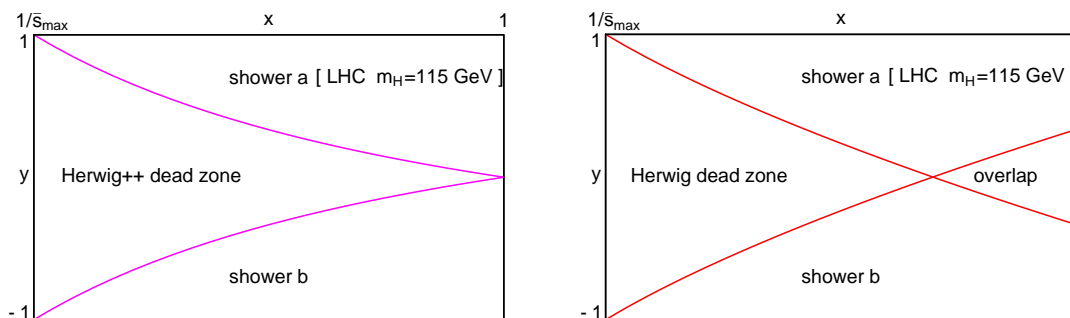

Figure 7. The *full* radiative phase space is given by the black rectangle in the x, y plane, bounding the plots on the right. The minimum kinematically allowed value of x is shown as $1/\bar{s}_{\max} = p^2/s$. The region into which two colour connected partons a and b cannot emit radiation, according to the Herwig++ and HERWIG shower algorithms, is marked 'dead zone' on the left- and right-hand plots respectively. In both algorithms, radiation into this dead zone is only possible with the help of a *hard matrix element correction*. Unlike Herwig++, in the case of the HERWIG algorithm there is a region of phase space which is double counted by the showering from a and b marked 'overlap'; this double counting is ultimately corrected for by a veto procedure. These plots correspond specifically to the case of a 115 GeV Higgs boson being produced via the gluon fusion process at LHC energies, although their form does not change significantly for the other processes we consider.

In general, given a leading-order configuration, one must first specify starting scales for each parton to evolve down from. The guiding principle behind the choice of starting scales in the HERWIG and Herwig++ angular-ordered shower algorithms is as follows: given two colour connected *shower progenitor partons* a and b, progenitor a cannot emit any *soft* radiation into the hemisphere defined by the direction of progenitor b, in the rest frame of

a and *b*, and *vice-versa*. This avoids any double counting of the phase space.[5] In other words, the starting scales are fixed by constraining that, in the limit of soft emissions, the two *jet regions*, of the first emission phase space (those which either progenitor can emit into) meet smoothly and do not overlap. If one then plots, in the full phase space, the contours to which these values of the evolution variables correspond to, one finds three regions: a jet region into which progenitor *a* can emit, a jet region into which progenitor *b* can emit and a further region into which neither can emit, the so-called *dead zone*. We show exactly these phase-space regions for the HERWIG [70, 71] and Herwig++ [44, 65] algorithms in figure 7, taking the case of gluon fusion at LHC energies as an example.

At this point we wish to remind the reader that in the distributions of $y_{\text{jet}} - y_{\text{H}}$ and $y_{\text{jet}} - y_{\text{HV}}$ which follow, the region around zero corresponds to the emission of the jet at right angles to the colliding partons in the partonic centre of mass frame (eq. (5.1)). This in turn corresponds to the region either side of the line $y = 0$ in the phase map shown in figure 7, along which the volume of the dead zone is *maximised*.

In figure 8 we superimpose, on the x, y phase-space map of the gluon fusion process, four contours corresponding to constant values of p_T: 10 GeV, 40 GeV, 80 GeV and m_{H}. This was done for the three scenarios which we study using the Monte Carlo predictions, specifically, a Higgs boson mass of 160 GeV at Tevatron energies (1960 GeV), a Higgs boson mass of 115 at LHC energies (14 TeV) and finally a Higgs boson mass of 300 GeV, also at LHC energies. In doing this we see that restricting the phase space to regions with higher and higher p_T leads to the expected result, namely, that the dead zone begins to fill the allowed region.

For the three scenarios we consider, figure 8 shows that a cut of $p_T >$ 80 GeV already leads to a great reduction in the area of phase space populated by the shower, while for $p_T > m_{\text{H}}$ the allowed region is fully contained within the dead zone. Similar plots are obtained for the Higgs-strahlung process by simply replacing the Higgs boson mass used in the calculation of the gluon fusion phase space, by the typical mass of the colourless vector boson plus Higgs boson system (figure 2 shows this to be in the range 200-300 GeV). The maps in figures 7 and 8 are key to a good understanding of the results in sections 5.2.2, 5.2.3.

As noted earlier, the dead zone of phase space, into which the shower cannot emit, can be filled with the aid of a hard matrix element correction. This involves populating that region according to the single real emission matrix element squared [44, 72]. In principle this is a simple procedure, since the dead zone does not run into any singular regions of phase space:[6] given an underlying N-body configuration one selects whether an emission into the dead zone occurs according to the conditional probability,

$$\mathcal{P}_{\text{dead}}^{\text{HW}}\left(\Phi_B\right) = 1 - \exp\left[-\int_{\text{dead}} \mathrm{d}\Phi_R \, \frac{\widehat{R}\left(\Phi_B, \Phi_R\right)}{B\left(\Phi_B\right)}\right], \tag{5.2}$$

---

[5]In practice, in the case of HERWIG, there is a small amount of overlap in the phase space allotted to each shower progenitor, although the algorithm later corrects for this by a vetoing procedure.

[6]Although the 'throat' of the dead zone in Herwig++ touches the soft boundary, it does so only in a vanishing region of the dead zone phase space, which is anyway cut off by the gluon mass regulator used in the shower.
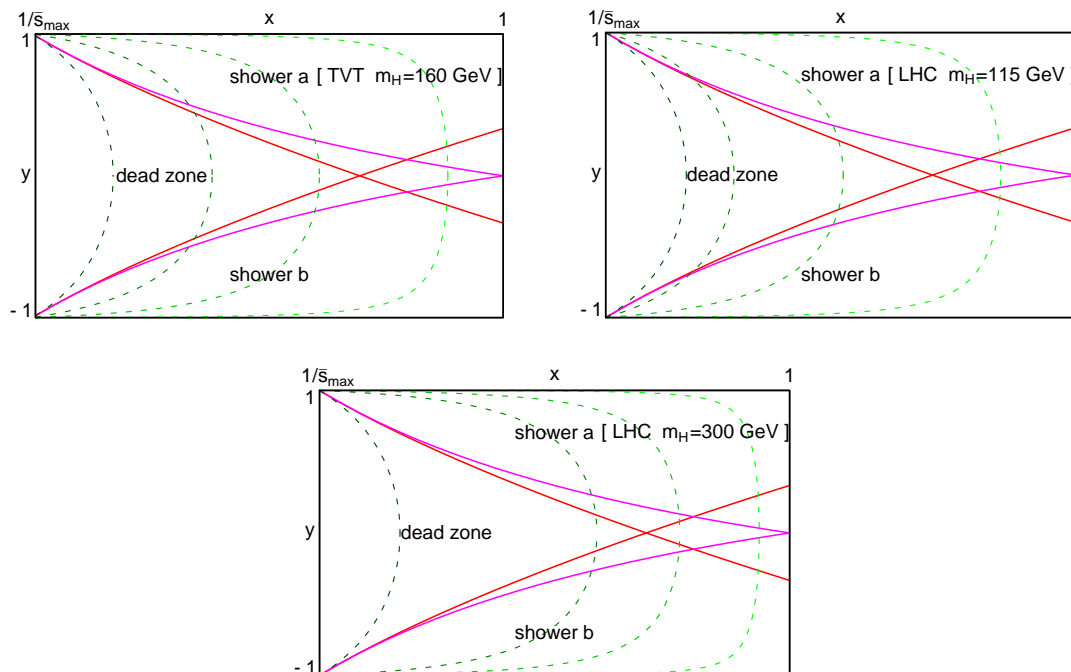
Figure 8. Radiative phase space in the x, y plane, as in figure 7 but with contours corresponding to constant values of p_T superimposed in green, from lightest to darkest (right to left) respectively these are, $p_T =$10 GeV, $p_T =$40 GeV, $p_T =$80 GeV and $p_T = m_H$. The region into which the two shower progenitors cannot emit radiation is again marked 'dead zone'; for HERWIG this area is bounded in red while for Herwig++ it lies between the magenta lines. The three plots correspond to the three scenarios under study in the remainder of the paper: a Higgs boson of mass 160 GeV at the Tevatron, a Higgs boson of mass of 115 GeV at the LHC, and a Higgs boson of mass 300 GeV also at the LHC. The area with emissions $p_T > m_H$ is entirely within the dead zone in all scenarios.

and, if an emission is to be generated, it is distributed according to the single real emission matrix element squared including PDFs $(R(\Phi_B, \Phi_R))$. Neglecting terms beyond NLO accuracy, $\mathcal{P}^{\mathrm{HW}}_{\mathrm{dead}}(\Phi_B)$, integrated over the Born variables, gives the fraction of the NLO cross section which the dead zone would contribute.

In all cases the hard matrix element correction is accompanied by a soft matrix element correction, which corrects the distribution of the hardest emission in the parton shower regions so that it is also given by $R(\Phi_B, \Phi_R)$. The combination of the soft and hard matrix element corrections ensures that, to $\mathcal{O}(\alpha_S)$, the distribution of real radiation is exactly matched either side of the dead zone boundaries, i.e. any sensitivity on the position of the dead zone boundary will be at the level of $\mathcal{O}(\alpha_S^2)$ terms, which should not be logarithmically enhanced since the boundary is predominantly in the high p_T region.

The same exact matching at $\mathcal{O}(\alpha_S)$ is true in the MC@NLO program, which feeds events to the HERWIG parton shower. In this case the generation of the first emission is done according to the full NLO differential cross section with additional, resummed, higher order corrections entering in the shower regions of the phase space. Sensitivity to the dead zone boundary is present in the NLO calculation through the shower subtraction

terms, which are required to avoid double counting of the NLO contributions through the subsequent showering with HERWIG. Ultimately, in MC@NLO, one has that the emission rate in the shower regions is given by the resummed rate in the shower's Sudakov form factor, corrected at $\mathcal{O}(\alpha_{\mathrm{S}})$, while in the dead zone it is related to the fraction which that area contributes to the total NLO cross section. This is much like the case of the matrix element correction procedure and, as with that method, any mis-match between the shower region and the dead zone should therefore again relate to unenhanced $\mathcal{O}(\alpha_{\mathrm{S}}^2)$ terms. We stress that, unlike the matrix element correction method, the MC@NLO program includes also exact NLO virtual corrections to the process in the event generation process, giving full NLO accuracy. However, as we now wish to focus on the shapes of the distributions sensitive to the effects of real radiation, neglecting the overall normalisation, differences arising from virtual corrections only enter the results through terms beyond NLO accuracy. This last point is addressed further at the beginning of section 5.2.2.

As we have already described in sections 2 and 4, the POWHEG method generates the hardest emission completely independently of the detailed workings of the shower, it may be considered as being a p_T ordered shower in its own right, albeit for a single emission. Unlike the other methods, POWHEG therefore has no dependence whatsoever on the dead zone boundary and the way in which it generates the hardest emission generation is the same throughout the whole phase space.

5.2.2 Gluon fusion

In this subsection we compare our POWHEG simulation against predictions from the bare angular-ordered parton shower in Herwig++, the Herwig++ parton shower including matrix element corrections and MC@NLO. We also compare against a further prediction from the matrix element correction (MEC) procedure, in which we decrease the rate of emission into the dead zone by unenhanced terms of $\mathcal{O}(\alpha_S^2)$, by changing the denominator in $\mathcal{P}_{\mathrm{dead}}^{\mathrm{HW}}(\Phi_B)$ from $B(\Phi_B)$ to $\overline{B}(\Phi_B)$:

$$\mathcal{P}_{\mathrm{dead}}^{\mathrm{HW}}(\Phi_B) \rightarrow \mathcal{P}_{\mathrm{dead}}^{\mathrm{NLO}}(\Phi_B) = \int_{\mathrm{dead}} \mathrm{d}\Phi_R \, \frac{\widehat{R}(\Phi_B, \Phi_R)}{\overline{B}(\Phi_B)}. \tag{5.3}$$

Whereas integrating $\mathcal{P}_{\mathrm{dead}}^{\mathrm{HW}}(\Phi_B)$ over the Born variables gives the fraction of the NLO cross section contributed by the dead zone neglecting higher order terms, performing the same integral with $\mathcal{P}_{\mathrm{dead}}^{\mathrm{NLO}}(\Phi_B)$ gives this fraction *exactly*.[7] Although it should be obvious to the reader that this is technically only an alteration at the level of terms beyond NLO accuracy, we do not wish to give the impression that it is *a priori* a small change, at least not for the gluon fusion process (recall figure 1). We expect that this alteration should mean that the modified MEC predictions should reproduce well the rate at which MC@NLO emits radiation into the dead zone.

In figure 9 we show the p_T spectrum of the Higgs boson and also that of the hardest jet. One can see that the p_T spectra at the Tevatron are less hard than those obtained at the LHC, as one would expect given the greater centre-of-mass energies of the latter. One also

---

[7]For this reason we choose to distinguish the modified probability by the superscript NLO.

expects that, at the LHC, the larger mass of a 300 GeV Higgs boson would automatically give rise to it having a harder spectrum than that of a 115 GeV Higgs boson, this is indeed the case for all five Monte Carlo predictions.

In each of our three phenomenological scenarios we see that the behaviour of the different simulations is more-or-less the same with respect to one another. The effect of the radiation dead zone is very clear as a sharp *knee* in the spectra from the uncorrected Herwig++ parton shower (black dotted lines), as the transverse momentum approaches the Higgs boson mass. Only the effects of multiple emission mean that this is not an abrupt cut off (figure 8). As predicted, turning on the MECs and hence filling the dead zone in Herwig++, leads to a spectrum in much better agreement with all of the other methods (black lines). A very slight kink is still visible in this default MEC prediction, which we already forecast in section 5.2.1 as a mis-match, at $\mathcal{O}\left(\alpha_{\mathrm{S}}^2\right)$, across the dead zone boundary.

The modified MEC (green dotted lines) shows a similar trend with respect to the uncorrected parton shower prediction, although it comes as no surprise that it has a softer spectrum than the regular MEC, simply because the rate of emission into the dead zone is reduced by an amount approximately given by the NLO K-factor *cf.* eqs. (5.2), (5.3). From our earlier investigations concerning the dead zone one should expect that the difference in the emission rates in eqs. (5.2) and (5.3) directly manifests itself as the same relative difference in the upper values of the p_T spectra of the Higgs boson and the leading jet. This is indeed seen to be the case in figure 9, where the unmodified MEC prediction is around a factor of two higher than the modified one on the right-hand side of each plot.

In all cases the Herwig++ NLO POWHEG prediction (red lines) is seen to be in very close agreement with the predictions obtained using the normal MEC procedure (black lines). As we shall discuss more in section 5.3, we attribute this to the fact that the emission rates for the MEC method and the POWHEG implementation can be expected to converge to the same value at high p_T.

The MC@NLO p_T spectra are in general somewhat softer than those of the MEC procedure and POWHEG NLO prediction, they tend to lie between the prediction obtained using the modified MEC (green dotted lines) and the Herwig++ POWHEG/default MEC lines. Good agreement between the MC@NLO and modified MEC predictions can be seen for the case of a 115 GeV Higgs boson at the LHC, similarly, the agreement in the case of the Tevatron is good below 200 GeV, however, for a 300 GeV Higgs boson at the LHC the agreement is not as good as hoped beyond $p_T \simeq m_{\mathrm{H}}$. We suggest that these discrepancies arise from presence of an improvement introduced between versions 3.2 and 3.3 of MC@NLO, with the aim of improving the description of the Higgs boson p_T spectrum [22].

In figures 10 and 11 we show the distribution of the rapidity difference between the leading jet and the Higgs boson, for increasingly hard cuts on the p_T of the jet. Starting again with the bare parton shower prediction (black dotted lines), for each scenario and each value of the p_T cut on the leading jet, the structure is broadly the same, the distribution rises from the tails at either side of the plot into a hump before falling again into a very deep dip in the centre, at $y_{\mathrm{jet}} - y_{\mathrm{H}} = 0$.

These *volcano* formations are a direct manifestation of the radiation dead zone; the volume of the dead zone is maximised along the direction corresponding to wide angle
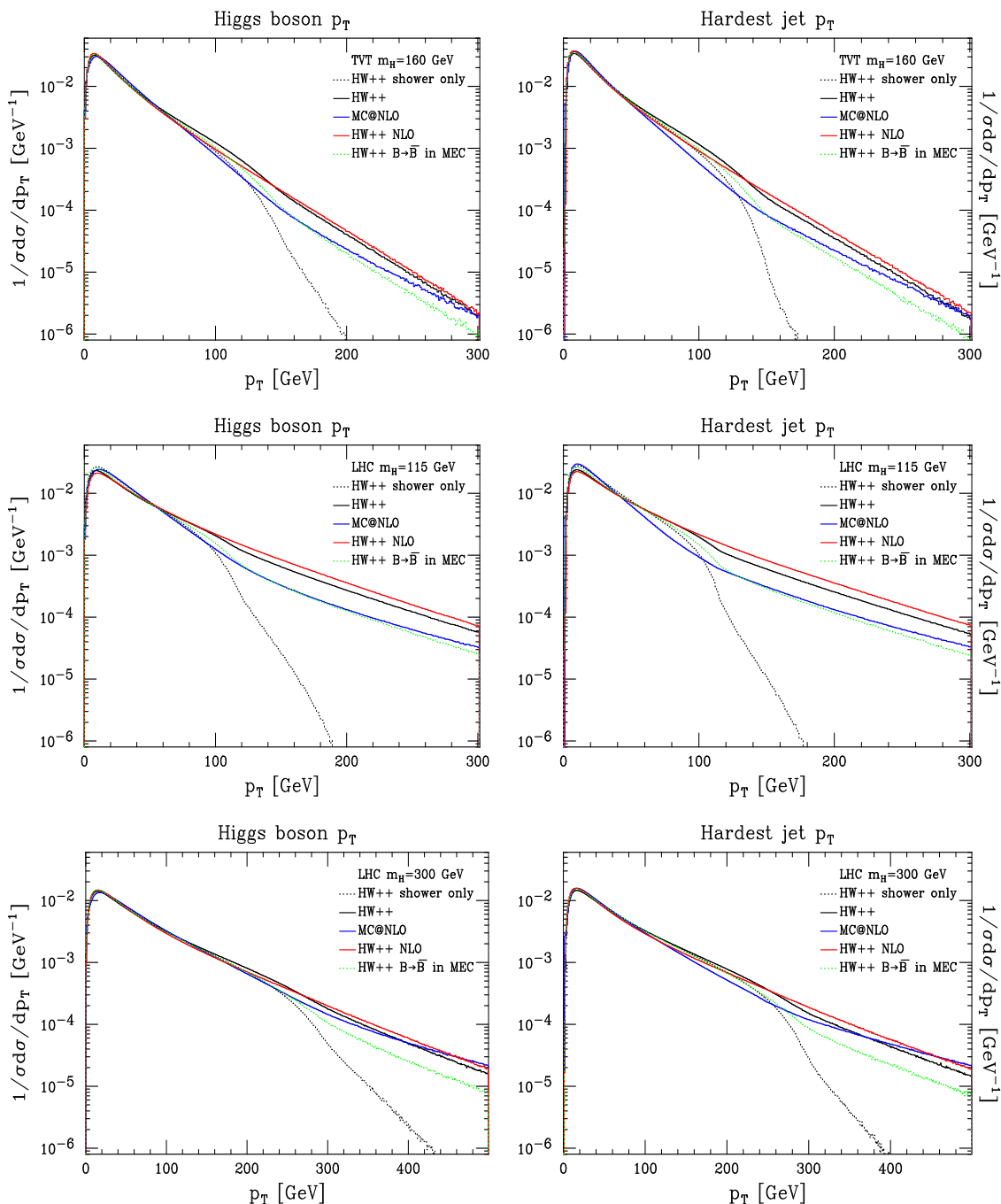
Figure 9. Transverse momentum spectra for the Higgs boson and the leading, highest p_T, jet, obtained using Herwig++ with matrix element corrections (black), Herwig++ without matrix element corrections, i.e. the uncorrected parton shower (dotted), MC@NLO (blue) and our POWHEG simulation inside Herwig++ (red). The green curve is obtained by modifying the hard component of the matrix element corrections, to decrease the amount of radiation produced in the associated high p_T, wide-angle, dead-zone, by terms beyond next-to-leading-order accuracy. This modification is discussed further in section 5.3.
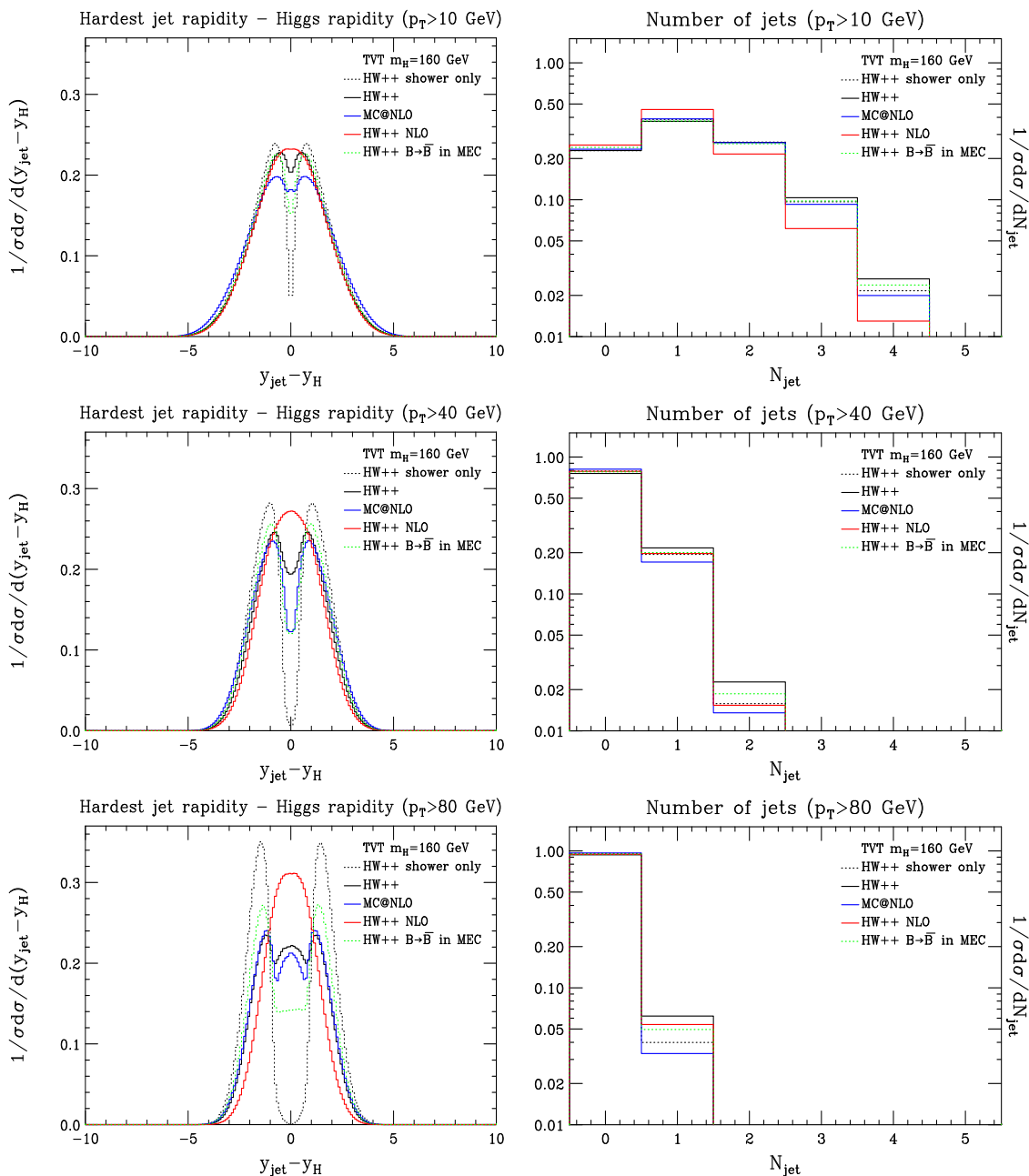
Figure 10. In the left hand column we show distributions of the difference in rapidity between the leading jet and a Higgs boson of mass 160 GeV at the Tevatron, for increasing cuts on the p_T of the leading jet. For a single emission, in the region close to zero, this variable is proportional to the angle between the emitted parton and the transverse direction in the partonic centre-of-mass frame (eq. (5.1)). In the right hand column we show the corresponding jet multiplicity distributions. The black and dotted lines show the predictions obtained using Herwig++ with and without matrix element corrections, respectively. The blue line shows the prediction from MC@NLO and the red line is that of our POWHEG simulation in Herwig++. The green line is obtained using a modified version of the hard matrix element correction, effectively decreasing the amount of radiation that this method produces in the high p_T, dead zone, by terms beyond NLO accuracy (see section 5.3).
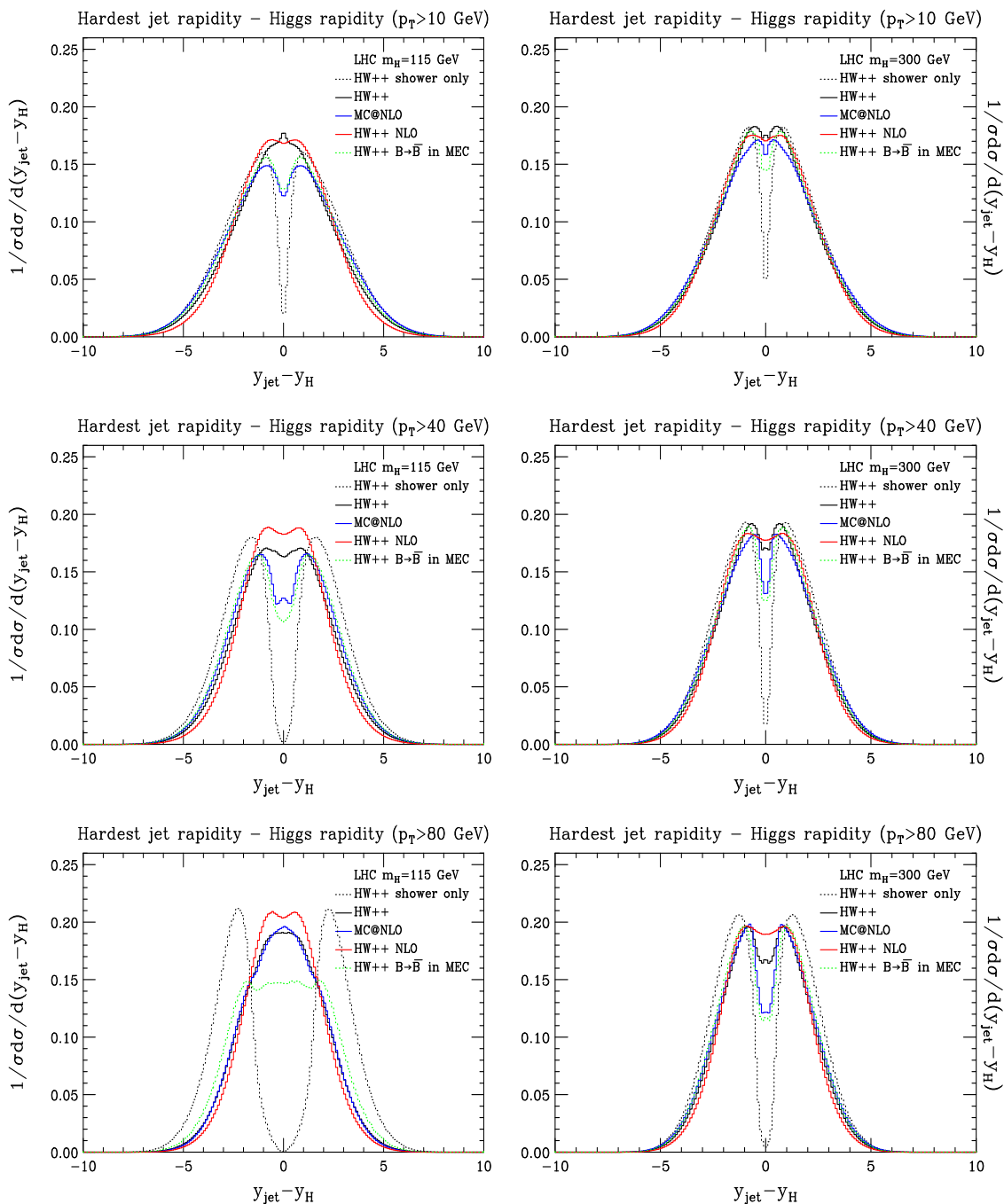
Figure 11. Distributions of the difference in rapidity between the leading jet and the Higgs boson in the gluon fusion process at the LHC, for increasing cuts on the p_T of the leading jet. The series of plots on the left hand side are obtained for a Higgs boson of mass 115 GeV, while those on the right correspond to a Higgs boson of mass 300 GeV. The colour assignment of the various predictions is described inset, it is the same as for earlier Tevatron predictions in figure 10.

radiation in the partonic centre-of-mass frame, $y \approx 0$, $\theta \approx \frac{\pi}{2}$ (section 5.2.1, figures 7, 8) and the $y_{jet} - y_H$ variable is proportional to $\theta - \frac{\pi}{2}$ (section 5.2, eq. (5.1)). The only thing

which may then be slightly surprising is that the distribution does not in fact go exactly to zero at $y_{jet} - y_H = 0$, this is simply due to the effects of multiple emissions (the phase space in figures 7 and 8 is only exact for the case of a single emission).

Looking in more detail at the structure of the uncorrected Herwig++ predictions, we see that the throat in each of volcano distributions widens as the p_T cut on the hardest jet is increased. This broadening occurs because the dead zone accounts for *proportionally* more and more of the smaller/less wide angle regions of the phase space as the p_T increases. This trend of the broadening throat with the hardening of the p_T cut is therefore visible in each of the three scenarios we consider and it will come as no surprise that the same occurs for the Higgs-strahlung process.

The hard matrix element correction begins to fill in the central throat region by emitting wide angle radiation into the dead zone. Nevertheless, both the modified and unmodified MEC results carry some residual sensitivity to the dead zone boundary, as evidenced by their inheritance of dips in the central region, dips which follow the same trend as that set by the uncorrected parton shower, to broaden and deepen as the p_T cut on the hardest jet is increased. We attribute this dip behaviour as being almost entirely due to the mismatch in the emission rate across the dead zone boundary, which occurs for terms beyond NLO accuracy, as discussed in section 5.2.1. This conclusion may not appear to hold for the 115 GeV Higgs boson when the p_T cut on the jet reaches 80 GeV. However, in this plot, the absence of a dip actually reinforces our assertion, as can be seen by consulting the 80 GeV p_T contour in the corresponding phase-space map; this contour shows that the allowed region for emissions is almost identically in the dead zone, so any matching across the dead zone boundary and, conversely, any mis-matching, is extremely limited in this special case.

Having understood how the dead zone is manifest in the rapidity difference plots, the differences observed between the modified and unmodified MEC methods are rather unremarkable: since the emission rate of the modified MEC into the dead zone is reduced by around a factor of two with respect to the unmodified correction, the former emits more wide angle radiation and so populates the central region of the $y_{jet} - y_H$ to a greater extent.

Although the HERWIG program has a slightly different phase-space coverage for its parton showers (figures 7, 8), they are apparently not so different, particularly away from the soft region. Considering the region of the phase space allowed by just a 10 GeV p_T cut (figure 8) it is already clear that the coverage by HERWIG and Herwig++ is really very similar and that it is basically identical by the time the cut reaches 80 GeV. The predictions of the uncorrected HERWIG shower, which showers the positive and negative unit weight events fed to it from MC@NLO, will then be very similar to those shown here for Herwig++, in particular, the volcano structures in the $y_{jet} - y_H$ distributions. This being the case, it is understandable that the MC@NLO distributions (blue lines) also exhibit dips in the central region, and that the behaviour of these dips with the varying p_T cut follows that of the MEC method; we also note that a number of these results are markedly similar to those obtained using the modified MEC.

Before discussing the POWHEG results we reiterate that this method is wholly independent of the details of the partitioning of phase space in the shower algorithms, it generates

the NLO emission effectively as a self contained p_T ordered parton shower, albeit with NLO accuracy, and thereby circumvents such issues. Hence, the appearance of a slight dip in the distributions of $y_{jet} - y_H$ cannot be explained in the same way as those seen in the predictions of the Herwig++ shower, with or without the MECs, nor those of MC@NLO. The central dip appearing in the POWHEG results alters the height of these distributions, in all cases, by less than 5%, it is therefore characteristic of the uncertainties typical of *NNLO* calculations, and is many times smaller than those seen in the other predictions. Given the smallness of the effect, its absence in the Tevatron distributions, and also the fact that it exhibits no discernible response to the changing p_T cut, we cannot comment on its origin.

Finally we note that only the POWHEG predictions clearly exhibit the expected physical behaviour on increasing the p_T cut: that the $y_{jet} - y_H$ distribution should become *squeezed* toward the central region, as the phase space available for small angle emissions, which populate the tails, becomes reduced relative to the phase space available for wide angle emissions. This trend is somewhat obscured in the distributions predicted by the other methods.

At this point we do not wish to give the impression that the dips exhibited by the MEC and MC@NLO predictions are incorrect. It is our contention, however, that these predictions can be consistently explained by ascribing the origin of the dips to a mismatch at $\mathcal{O}\left(\alpha_S^2\right)$ in the emission rates either side of the dead zone boundary. Although the dead zone boundary is an unphysical partition in the phase space, we stress that the mis-match involves terms beyond the stated accuracy of either method. Looking ahead, beyond NLO accuracy, it should then be the case that the MEC and MC@NLO approaches fail to approximate any higher order terms, while the POWHEG method, being independent of any kind of artificial phase space partitioning, should fare much better.

In figure 10 we also show jet multiplicity distributions associated to each of the Tevatron $y_{jet} - y_H$ plots. As expected, these plots show, in all cases, that the jet multiplicity distribution decreases rapidly as the p_T cut on the leading jet is increased, with only $\sim 5\%$ of events containing a jet once the cut reaches $80\,\mathrm{GeV}$. In the case of the soft p_T cut ($p_T \text{¿} 10\,\mathrm{GeV}$) one can see that the POWHEG approach predicts events with lower multiplicity than the other methods (which broadly agree with one another).

5.2.3 Higgs-strahlung

In figure 12 we compare the transverse momentum spectra of the Higgs boson and W boson assuming a $160\,\mathrm{GeV}$ Higgs boson mass at the Tevatron and Higgs boson masses of $115\,\mathrm{GeV}$ and $300\,\mathrm{GeV}$ at the LHC. In each case we compare the results obtained using the uncorrected Herwig++ parton shower, the parton shower with MECs, MC@NLO and our POWHEG implementation. All four approaches agree remarkably well. The fact that the uncorrected, leading-order, parton shower prediction agrees so well with the other methods, which include at least the NLO real emission corrections, indicates that these distributions are rather insensitive to the emission of additional radiation, therefore one should not expect to see differences among the more sophisticated approaches.

On the right of figure 13 we show the rapidity of the leading jet in $q\bar{q} \rightarrow ZH$ events. These rapidity distributions are concentrated more in the central region in the case of the Tevatron than the LHC. This behaviour can be inferred from the fact that there is more phase space available for extra radiation at LHC energies. The same line of reasoning also explains why the rapidity distribution in the case of the 300 GeV Higgs boson at the LHC is also more central than that of the 115 GeV Higgs boson. There is a tendency in all of the plots for the MC@NLO distributions to contain more events in the tails, conversely, the POWHEG results show more jets produced in the central region. The predictions from the uncorrected parton shower and the parton shower with a MEC lie between those of MC@NLO and POWHEG, with the former being slightly closer to MC@NLO and the latter closer to POWHEG.

The plots on the left of figure 13 are a more interesting test of our methods, they show the transverse momentum of the colourless Z-Higgs boson system and also the rapidity of the hardest jet in the same $q\bar{q} \rightarrow ZH$ events. The p_T of the vector boson plus Higgs boson system is generated directly by the Higgs-strahlung POWHEG simulation. As in the case of the gluon fusion process we see that the POWHEG results and those of the parton shower including matrix element corrections are essentially the same, and that both are harder than the corresponding MC@NLO prediction. However, the degree by which the latter predictions are above those of MC@NLO is significantly reduced with respect to that seen in the gluon fusion case. We again attribute this to the relative differences in the rate of emission into the dead zone, in the MEC method this occurs with probability $\mathcal{P}_{\text{dead}}^{\text{HW}}(\Phi_B)$ (eq. (5.2)) while in MC@NLO the analogous probability will be essentially given by the fraction which the dead zone contributes to the total NLO cross section i.e. $\mathcal{P}_{\text{dead}}^{\text{NLO}}(\Phi_B)$ (eq. (5.3)). Since the denominators in these emission probabilities differ by an amount of order the NLO K-factor the differences arising in the gluon fusion case should be large whereas they should be small in the Higgs-strahlung case. It is difficult to see it clearly at the upper end of these Higgs-strahlung p_T spectra but the MC@NLO result is below that of POWHEG and the MEC methods by roughly 30%, which is compatible with the enhancement due to the NLO corrections seen in the comparisons with MCFM in e.g. figure 2.

In figures 14 and 15 we show distributions of the rapidity differences $y_{\text{jet}} - y_{\text{ZH}}$ and $y_{\text{jet}} - y_{\text{WH}}$, for the $q\bar{q} \rightarrow WH$ and $q\bar{q} \rightarrow ZH$ processes, at the Tevatron and LHC respectively. These plots display the same features and trends as seen in the gluon fusion case. As before, the uncorrected parton shower predictions give rise to volcano shaped distributions due to the dead zone in the phase space and increasing the p_T cut on the leading jet again has the effect of broadening the throat, reflecting the fact that the dead zone occupies an increasingly large fraction of the allowed phase space.

The MEC and MC@NLO methods emit radiation into the dead zone, filling the throat region in the $y_{\text{jet}} - y_{\text{WH}}$ and $y_{\text{jet}} - y_{\text{ZH}}$ plots, however, they still exhibit a clear sensitivity to the dead zone boundary which is manifest as irregularities in the central regions of the distributions. For the case that the p_T cut on the leading jet is soft, $p_T > 10$ GeV, the MEC predictions show a tiny, sharp dip around the centre, while those of MC@NLO show the formation of a small tower in the same place. This is plainly a mis-match of $\mathcal{O}\left(\alpha_S^2\right)$ terms

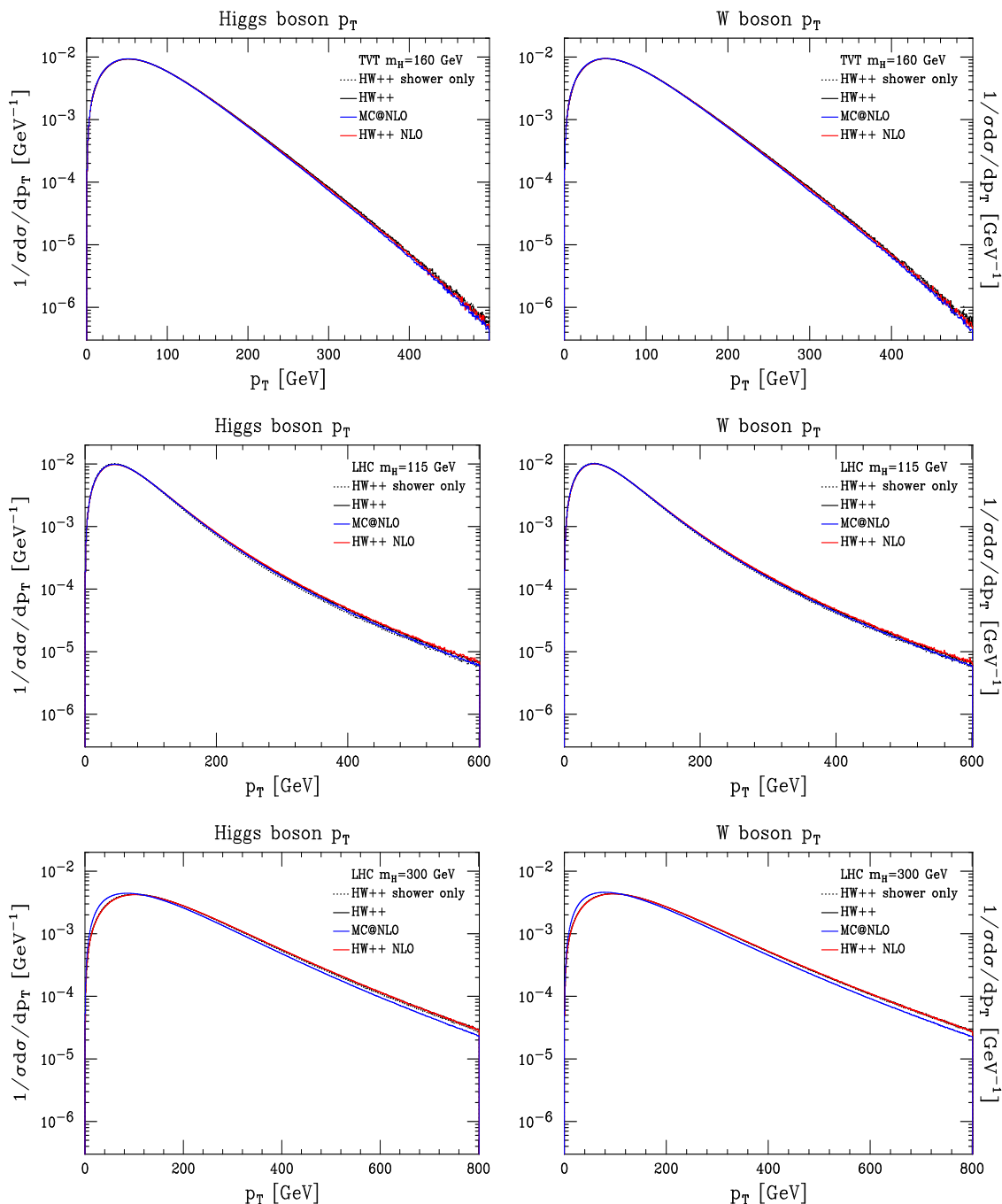**Figure 12**. Transverse momentum spectra for the Higgs boson (left) and the $W^\pm$ boson in $q\bar{q} \to HW^\pm$ events obtained using Herwig++ with and without matrix element corrections (black and black dots respectively), MC@NLO (blue) and our POWHEG simulation inside Herwig++ (red). The first uppermost predictions, for the Tevatron, are obtained assuming a Higgs boson mass of $160\,\mathrm{GeV}$. The following four plots are analogous projections for the LHC for Higgs boson masses of $115\,\mathrm{GeV}$ and $300\,\mathrm{GeV}$.

across the phase-space partition. As the p_T veto increases the dips in the MEC predictions tend to deepen and in the case of MC@NLO, the small towers turn to small dips. In all
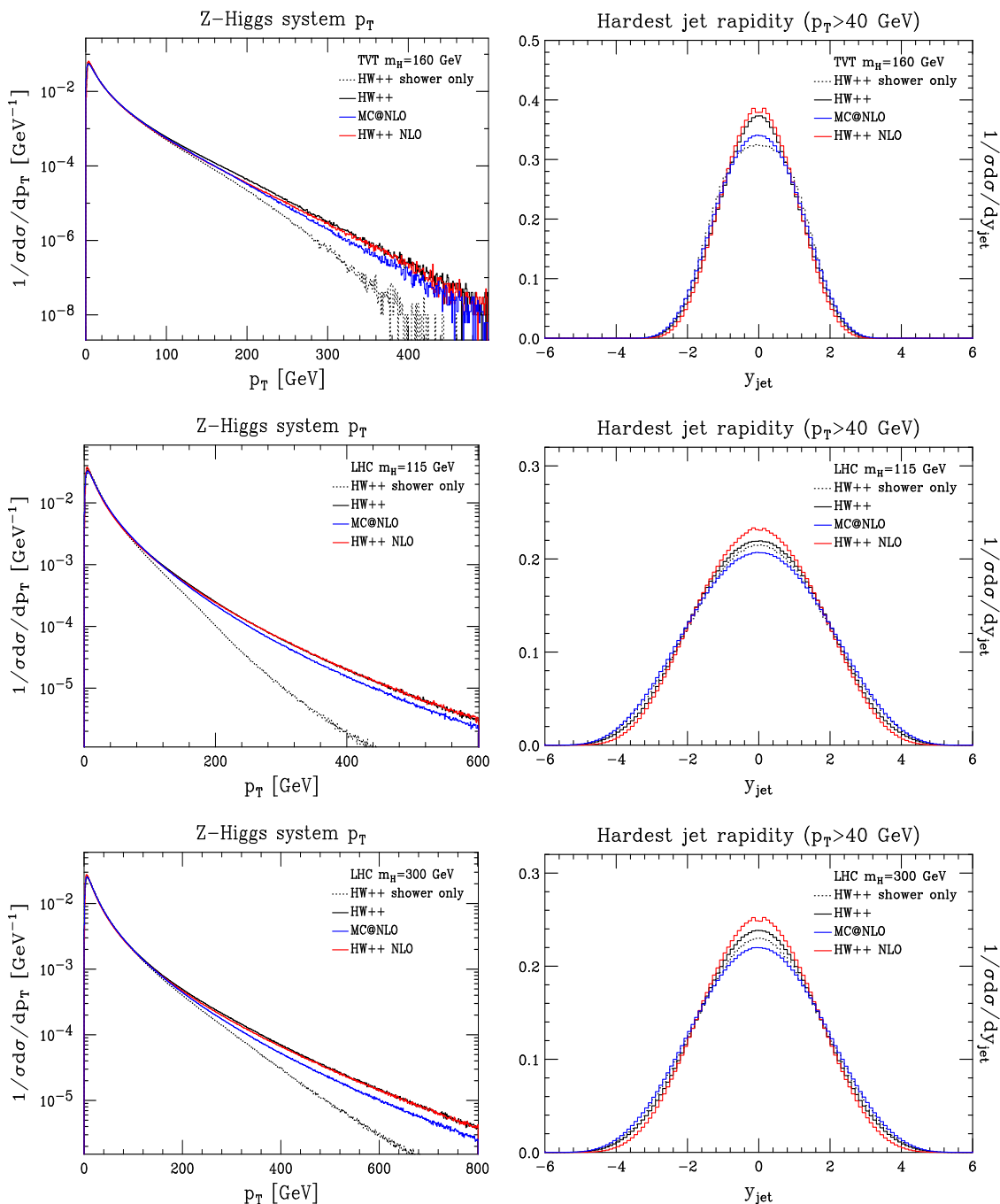
Figure 13. On the left we compare predictions for the transverse momentum spectrum of the colourless final-state system comprised of the Z and Higgs boson (left) in $q\bar{q} \to ZH$ events. From top to bottom, respectively, these results are obtained for Tevatron energies with a Higgs boson mass of 160 GeV, LHC energies with a Higgs boson mass of 115 GeV and LHC energies with a Higgs boson mass of 300 GeV. On the right hand side we show the corresponding distributions for the rapidity of the leading, highest p_T, jet. The colour assignment for the different approaches used is shown inset, and is the same as that in figure 12.

cases the POWHEG distributions are smooth, exhibiting no irregular *volcanic* features, as expected, furthermore they are more concentrated in the central region than all of the other predictions, indicating a tendency to emit proportionally more wide angle radiation.

We point out that in all of the MEC and MC@NLO predictions the residual effects of the phase-space dead zone are felt much less strongly in the case of Higgs-strahlung than in gluon fusion. These behaviours are less marked for the same reason that the MC@NLO and POWHEG p_T spectra agree better for Higgs-strahlung than for gluon fusion: the fact that the NLO corrections are substantially smaller for Higgs-strahlung means $\overline{B}(\Phi_B)$ is less different to $B(\Phi_B)$ and so the $\mathcal{O}(\alpha_S^2)$ differences in the rates at which each method populates the dead zone are greatly reduced, *cf.* eqs. (5.2), (5.3).

5.3 Emission rates in the dead zone

In this subsection we present an heuristic discussion of the rates with which each approach emits into the high p_T region. In particular we consider the area of phase space corresponding to transverse momenta $p_T > m_n$, where m_n is the mass of the colourless final-state system. This region is completely contained within the dead zone and the contribution which it makes to the cross section is not logarithmically enhanced (section 5.2.1).

From eq. (5.2) it follows that the probability for Herwig++ to generate an emission with $p_T > m_n$ is

$$\mathcal{P}_{m_n}^{\mathrm{HW}}(\Phi_B) = \int_{m_n} \mathrm{d}\Phi_{R_1} \frac{\widehat{R}_1(\Phi_B, \Phi_{R_1})}{B(\Phi_B)}, \tag{5.4}$$

where the omitted higher-order terms in the exponential series are negligible, not simply because they carry higher powers of the coupling constant but also, significantly, because the contribution to the total cross section from this region is in general very small. In eq. (5.4) $\widehat{R}_1(\Phi_B, \Phi_{R_1})$ is, as before, the real single-emission matrix element squared, including flux factors and PDFs, and Φ_B and Φ_{R_1} are the Born and radiative variables parametrising the two-body phase space. The lower limit on the integral signifies that it extends over all available phase space above $p_T > m_n$. Our adding a subscript '1' to each R, has no significance here but it will be useful later, in discussing NNLO corrections.

The fraction of MC@NLO events with emissions in this region is given by the corresponding fraction of the NLO cross section

$$\mathcal{P}_{m_n}^{\mathrm{NLO}}(\Phi_B) = \int_{m_n} \mathrm{d}\Phi_{R_1} \frac{\widehat{R}_1(\Phi_B, \Phi_{R_1})}{\overline{B}(\Phi_B)}. \tag{5.5}$$

For what follows it will be useful to note that if we expand the denominator in eq. (5.5), neglecting terms $\mathcal{O}(\alpha_S^3)$ and above, we have

$$\mathcal{P}_{m_n}^{\mathrm{NLO}}(\Phi_B) = \int_{m_n} \mathrm{d}\Phi_{R_1} \frac{\widehat{R}_1(\Phi_B, \Phi_{R_1})}{B(\Phi_B)} \left(2 - \frac{\overline{B}(\Phi_B)}{B(\Phi_B)}\right). \tag{5.6}$$

In POWHEG the Sudakov form factor, $\Delta_{\hat{R}}(p_T)$ in Eq (2.3), is the probability that no radiation is emitted from the leading-order partons in evolving from the maximum kinematically allowed transverse momentum, down to p_T. Hence a POWHEG simulation
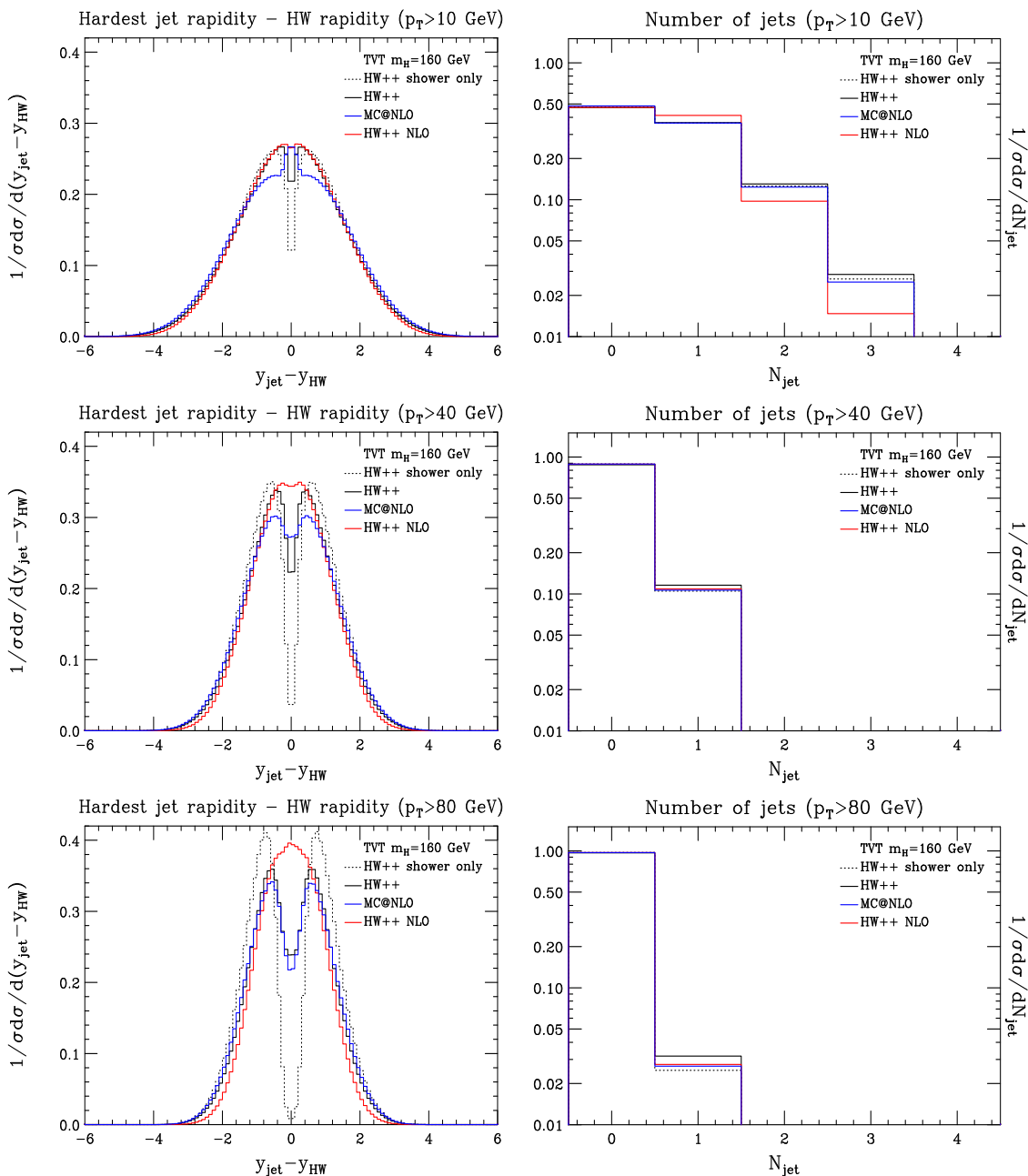
– 33 –

Figure 14. In the left-hand column are distributions of the difference in rapidity between the leading jet and the colourless W−Higgs boson system, in $q\bar{q} \rightarrow HW^{\pm}$ events at the Tevatron, for increasing cuts on the p_T of the jet. For a single emission, the central value $y_{\text{jet}} - y_{\text{HW}} = 0$ corresponds to a configuration where the W-Higgs boson and the colliding partons travel at right-angles in the partonic centre-of-mass frame (eqs. (3.9), (5.1)). In the plots on the right-hand side we show the corresponding jet multiplicity distributions. The black and dotted lines show the predictions obtained using Herwig++ with and without matrix element corrections respectively. The blue line shows the predictions of MC@NLO and the red line corresponds to our POWHEG simulation inside Herwig++.
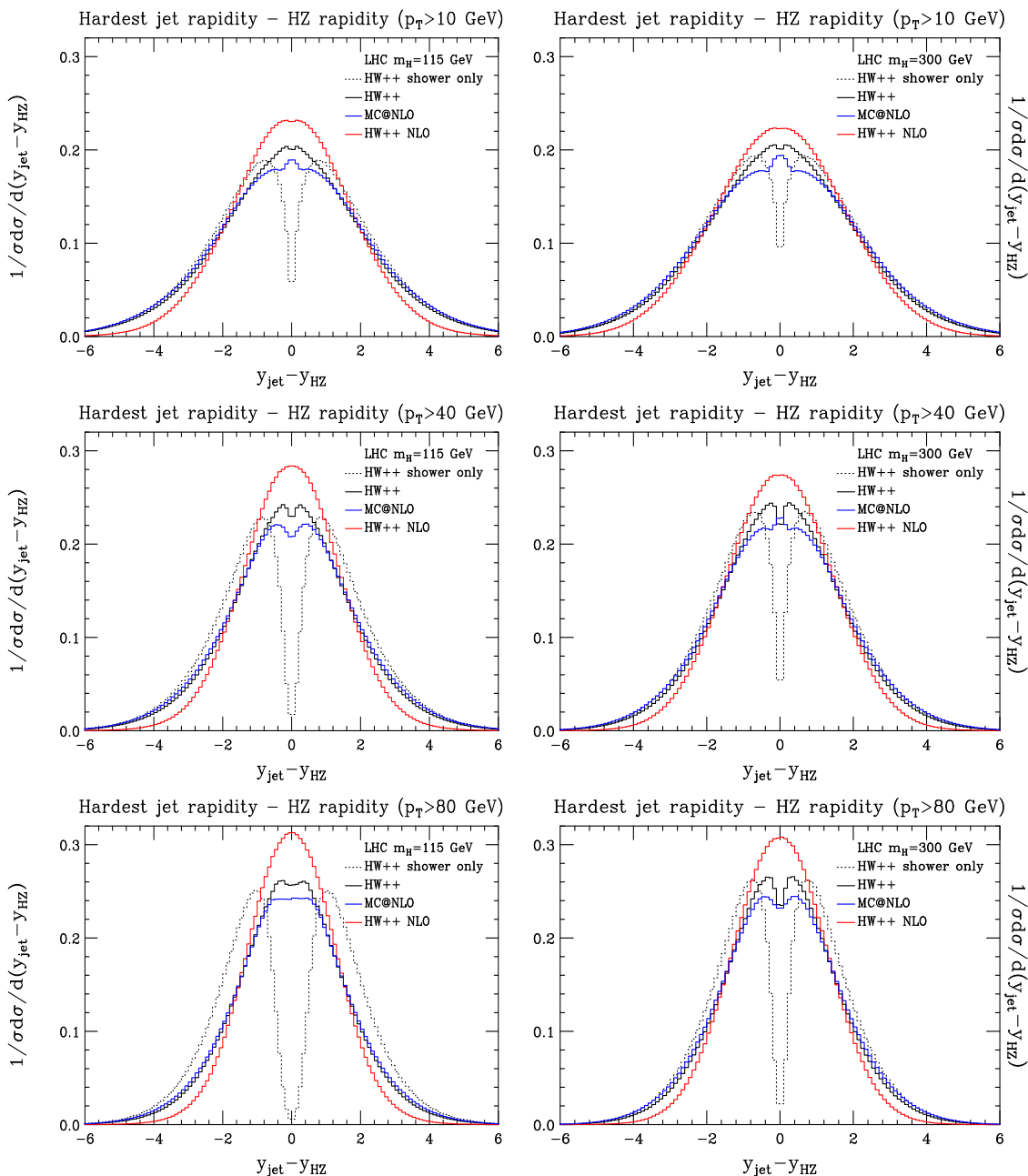
Figure 15. Distributions of the difference in rapidity between the leading jet and the Higgs boson in the $q\bar{q} \to ZH$ process at the LHC, for increasing cuts on the p_T of the leading jet. The series of plots on the left hand side are obtained for a Higgs boson of mass $115\,\mathrm{GeV}$, while those on the right correspond to a Higgs boson of mass $300\,\mathrm{GeV}$. The colour assignment of the various predictions is described inset, it is the same as for earlier Tevatron predictions for $q\bar{q} \to HW^{\pm}$ in Fig 14.

will emit radiation into the same high p_T region with probability $\mathcal{P}_{mn}^{\mathrm{PH}} = 1 - \Delta_{\hat{R}}\,(m_n)$. Neglecting kinematically suppressed $\mathcal{O}(\alpha_{\mathrm{S}}^2)$ terms, as in the case of the MEC, this gives,

$$\mathcal{P}_{mn}^{\mathrm{PH}} = \int_{m_n} \mathrm{d}\Phi_{R_1} \frac{\widehat{R}_1\,(\Phi_B, \Phi_{R_1})}{B\,(\Phi_B)}\,. \tag{5.7}$$

Comparing eqs. (5.4) and (5.7), we see that the emission rates in the high p_T region, from POWHEG and the MEC, are the same up to the scale used in the strong coupling constant (in the former it is p_T while in the latter it is m_T). These corresponding emission rates are evident in the p_T spectra in figures 9 and 13. It is also clear that MC@NLO will emit into this region less often than the other two since, whereas the POWHEG and Herwig++ simulations have an emission probability inversely proportional to the Born cross section $B(\Phi_B)$, the probability of emission in MC@NLO is inversely proportional to the, larger, NLO cross section, $\overline{B}(\Phi_B)$. This argument is also supported by what we have seen in the p_T spectra. Essentially we have

$$\mathcal{P}_{m_n}^{\mathrm{HW}} \approx \mathcal{P}_{m_n}^{\mathrm{PH}} \approx \mathcal{K}\,\mathcal{P}_{m_n}^{\mathrm{NLO}} \tag{5.8}$$

where $\mathcal{K}$ is the relevant NLO K-factor. For processes with smaller K-factors the differences in the population of the dead zone in each approach should not differ too much but MC@NLO will be systematically softer than POWHEG and Herwig++.

Is one of these probabilities more correct than the others? In ref. [41] the authors compared the Higgs boson p_T spectrum from their POWHEG simulation to NNLO predictions [55, 56] and found that they agreed better than those of MC@NLO. The amount of radiation produced in the high p_T dead zone in the case of the fixed order, NNLO, Monte Carlo used in ref. [41] should be the relevant fraction of the NNLO cross section

$$\mathcal{P}_{m_n}^{\mathrm{NNLO}}(\Phi_B) = \int_{m_n} \mathrm{d}\Phi_{R_1} \left[\widehat{R}_1(\Phi_B, \Phi_{R_1}) + R_{1+1}(\Phi_B, \Phi_{R_1}) + \int \mathrm{d}\Phi_{R_2}\, R_2(\Phi_B, \Phi_{R_1}, \Phi_{R_2}) \right]$$
$$\div\, \mathrm{d}\sigma_{\mathrm{NNLO}}(\Phi_B)\,, \tag{5.9}$$

where the sum of the last two terms in the numerator represents the *finite* combination of the one-loop single emission matrix element interfering with the tree-level single emission matrix element, and the squared double emission matrix element respectively, including PDF and flux factors. Since the numerator of $\mathcal{P}_{m_n}^{\mathrm{NNLO}}$ is $\mathcal{O}(\alpha_{\mathrm{S}})$, if we omit terms $\mathcal{O}(\alpha_{\mathrm{S}}^3)$ in $\mathcal{P}_{m_n}^{\mathrm{NNLO}}$ we can replace the NNLO differential cross section in the denominator by the NLO one (eq. (3.24)), whence it follows that

$$\mathcal{P}_{m_n}^{\mathrm{NNLO}}(\Phi_B) = \int_{m_n} \mathrm{d}\Phi_{R_1}\, \frac{\widehat{R}_1(\Phi_B, \Phi_{R_1})}{B(\Phi_B)} \left[1 - \frac{\overline{B}(\Phi_B)}{B(\Phi_B)} + \frac{\overline{R}_1(\Phi_B, \Phi_{R_1})}{\widehat{R}_1(\Phi_B, \Phi_{R_1})} \right], \tag{5.10}$$

where $\overline{B}(\Phi_B)$ was defined in eq. (2.2) and $\overline{R}(\Phi_B, \Phi_{R_1})$ is defined analogously as

$$\overline{R}_1(\Phi_B, \Phi_{R_1}) = \widehat{R}_1(\Phi_B, \Phi_{R_1}) + R_{1+1}(\Phi_B, \Phi_{R_1}) + \int \mathrm{d}\Phi_{R_2}\, R_2(\Phi_B, \Phi_{R_1}, \Phi_{R_2})\,. \tag{5.11}$$

Whereas the NNLO rate has $\overline{R}_1$ in the numerator *all* of the others just contain the term corresponding to the squared single emission matrix element $\widehat{R}_1$. Replacing $\overline{R}_1 \to \widehat{R}_1$ in eq. (5.10) gives eq. (5.6). We can consider $\overline{B}/B$ and $\overline{R}_1/\widehat{R}_1$ as K-factors for the processes $gg \to H$ and $gg \to H + \mathrm{jet}$, differential in Φ_B and $\{\Phi_B, \Phi_{R_1}\}$, respectively. One can see from eqs. (5.7) and (5.10) that if these two K-factors coincide so too will the rates for the POWHEG and NNLO calculations. In fact this seems to be more-or-less the case for

$gg \to H$ and $gg \to H + \text{jet}$ processes, which have very similar K-factors of around 1.6 / 1.7 [73]. It then seems quite feasible that the p_T spectrum of the Higgs boson in gluon fusion should be better modelled by the POWHEG approach, as was found to be the case in ref. [41].

Equation (5.10) does not tell us that POWHEG will *generally* reproduce higher orders better than MC@NLO. According to eq. (5.10) if $\overline{R}_1/\widehat{R}_1$ is more-or-less one and $\overline{B}/B$ is significantly greater than one then MC@NLO will give a better estimate of $\mathcal{P}_{m_n}^{\mathrm{NNLO}}$ than the POWHEG approach.

6 Conclusion

In this work we have fully realized the POWHEG NLO matching prescription for Higgs boson production via gluon fusion and Higgs-strahlung processes, within the Herwig++ Monte Carlo event generator, including truncated shower effects to correctly include colour coherence.

The cross sections and parton level NLO distributions were found to be in very good agreement with the MCFM NLO Monte Carlo. The shapes of the emission spectra from the full simulation, including parton shower effects, are seen to broadly agree well with the older matrix element correction method and also MC@NLO.

We observe that the p_T spectra from the MC@NLO program tend to be softer than those of POWHEG and the matrix element correction method. We ascribe this effect to differences, at the level of $\mathcal{O}\left(\alpha_{\mathrm{S}}^2\right)$ terms, beyond the stated accuracy of all approaches, in the rate at which they emit radiation into the so-called *dead zone*, associated to high p_T and wide angle emissions. We have been able to estimate the magnitude of the relative difference with a fair degree of success and, based on this line of reasoning, we presented an argument for why the POWHEG method appears to better reproduce the NNLO Higgs boson p_T spectrum in gluon fusion.

Separately, we have shown that a mis-match between terms of this magnitude manifests itself as marked sensitivity to the unphysical dead zone partition, for the predictions of the rapidity difference distributions $y_{\mathrm{jet}} - y_{\mathrm{H}}$ and $y_{\mathrm{jet}} - y_{\mathrm{VH}}$, for both the matrix element correction method and MC@NLO. These distributions acquire irregularities in the central region corresponding to wide angle emissions. This would seem to rule out the possibility of these two methods giving a good approximation of unenhanced NNLO effects in these distributions. Conversely, the POWHEG predictions for these distributions are smooth and physical in appearance, by construction, they have no sensitivity to the dead zone partition.

At present there is no known method of consistently including exact NNLO fixed order calculations within a parton shower simulation. An approximate means of doing this, involving the reweighting of PYTHIA [64] and MC@NLO events such that they reproduce certain NNLO distributions, has been recently carried out in ref. [74]. Based on the findings discussed above, it is our expectation that applying the same reweighting technique to POWHEG events should lead to further improvements in those predictions.

Both the gluon fusion and Higgs-strahlung simulations we have presented here are already available in Herwig++2.3. The algorithm we have used to implement the POWHEG

formalism, specifically that part concerning the *inverse mapping* of the hardest emission kinematics to a set of shower variables has further applications in multi-leg matching procedures e.g. the CKKW method [35, 36]. Likewise, the general formulae leading to eqs. (3.4), (3.24), for the phase space and differential cross-section for $a + b \rightarrow n$, can be readily used to implement other NLO calculations such as those in refs. [58–60]. This work is already at an advanced stage and will appear in the forthcoming version of Herwig++.

Acknowledgments

A Regularized and unregularized splitting functions

This appendix contains the splitting functions needed in the NLO calculations. The bare (spin averaged) splitting functions in $n = 4 - 2\epsilon$ dimensions are of the form

$$\hat{P}_{i,\widetilde{ic}}(x;\epsilon) = \hat{P}_{i,\widetilde{ic}}(x) + \epsilon \hat{P}^{\epsilon}_{i,\widetilde{ic}}(x) ,$$

where

$$\hat{P}_{gg}(x) = 2C_A \left[\frac{x}{1-x} + \frac{1-x}{x} + x(1-x) \right], \qquad \hat{P}^{\epsilon}_{gg}(x) = 0,$$

$$\hat{P}_{qq}(x) = C_F \left[\frac{1+x^2}{1-x} \right], \qquad \hat{P}^{\epsilon}_{qq}(x) = -C_F(1-x),$$

$$\hat{P}_{qg}(x) = C_F \left[\frac{1+(1-x)^2}{x} \right], \qquad \hat{P}^{\epsilon}_{qg}(x) = -C_F x,$$

$$\hat{P}_{gq}(x) = T_R \left[1 - 2x(1-x) \right], \qquad \hat{P}^{\epsilon}_{gq}(x) = -2T_R x(1-x) + \mathcal{O}(\epsilon) .$$

We write the 'customary' regularized Altarelli-Parisi equations kernels using the ρ-distributions as

$$P_{i,\widetilde{ic}}(x) = P^{\rho}_{i,\widetilde{ic}}(x) + C_{i,\widetilde{ic}} \left(p_{i,\widetilde{ic}} + 4\ln\eta \right) \delta(1-x) ,$$

where

$$P_{gg}^{\rho}\left(x\right) = 2C_A \left[\frac{x}{(1-x)_{\rho}} + \frac{1-x}{x} + x\left(1-x\right) \right], \qquad C_{gg} = C_A, \qquad p_{gg} = \frac{2\pi b_0}{C_A},$$

$$P_{qq}^{\rho}\left(x\right) = C_F \left[\frac{1+x^2}{(1-x)_{\rho}} \right], \qquad\qquad\qquad\qquad C_{qq} = C_F, \qquad p_{qq} = \frac{3}{2},$$

$$P_{qg}^{\rho}\left(x\right) = C_F \left[\frac{1+(1-x)^2}{x} \right],$$

$$P_{gq}^{\rho}\left(x\right) = T_R \left[x^2 + (1-x)^2 \right],$$

and

$$b_0 = \frac{1}{4\pi} \left(\frac{11}{3} C_A - \frac{4}{3} T_R n_{\mathrm{lf}} \right),$$

with all other $p_{i,\widetilde{ic}}$ and $C_{i,\widetilde{ic}}$ being equal to zero.

References

[1] F. Englert and R. Brout, *Broken symmetry and the mass of gauge vector mesons*, *Phys. Rev. Lett.* **13** (1964) 321 [SPIRES].

[2] P.W. Higgs, *Broken symmetries and the masses of gauge bosons*, *Phys. Rev. Lett.* **13** (1964) 508 [SPIRES].

[3] G.S. Guralnik, C.R. Hagen and T.W.B. Kibble, *Global conservation laws and massless particles*, *Phys. Rev. Lett.* **13** (1964) 585 [SPIRES].

[4] T.W.B. Kibble, *Symmetry breaking in non-Abelian gauge theories*, *Phys. Rev.* **155** (1967) 1554 [SPIRES].

[5] H.M. Georgi, S.L. Glashow, M.E. Machacek and D.V. Nanopoulos, *Higgs bosons from two gluon annihilation in proton proton collisions*, *Phys. Rev. Lett.* **40** (1978) 692 [SPIRES].

[6] ALEPH collaboration, *Precision electroweak measurements and constraints on the standard model*, arXiv:0811.4682 [SPIRES].

[7] A. Djouadi, *The anatomy of electro-weak symmetry breaking. I: the Higgs boson in the standard model*, *Phys. Rept.* **457** (2008) 1 [hep-ph/0503172] [SPIRES].

[8] J.R. Andersen, V. Del Duca and C.D. White, *Higgs boson production in association with multiple hard jets*, *JHEP* **02** (2009) 015 [arXiv:0808.3696] [SPIRES].

[9] J.M. Campbell, R.K. Ellis and G. Zanderighi, *Next-to-Leading Order Higgs + 2 jet production via gluon fusion*, *JHEP* **10** (2006) 028 [hep-ph/0608194] [SPIRES].

[10] V. Del Duca et al., *Monte Carlo studies of the jet activity in Higgs + 2 jet events*, *JHEP* **10** (2006) 016 [hep-ph/0608158] [SPIRES].

[11] S.L. Glashow, D.V. Nanopoulos and A. Yildiz, *Associated production of Higgs bosons and Z particles*, *Phys. Rev.* **D 18** (1978) 1724 [SPIRES].

[12] E. Eichten, I. Hinchliffe, K.D. Lane and C. Quigg, *Super collider physics*, *Rev. Mod. Phys.* **56** (1984) 579 [*Addendum ibid.* **58** (1986) 1065] [SPIRES].

[13] D0 collaboration, V.M. Abazov et al., *A search for associated W and Higgs boson production in p p̄ collisions at √s = 1.96 TeV*, *Phys. Rev. Lett.* **102** (2009) 051803 [arXiv:0808.1970] [SPIRES].

[14] CMS collaboration, G.L. Bayatian et al., *CMS technical design report, volume II: physics performance*, *J. Phys.* **G 34** (2007) 995 [SPIRES].

[15] J.M. Butterworth, A.R. Davison, M. Rubin and G.P. Salam, *Jet substructure as a new Higgs search channel at the LHC*, *Phys. Rev. Lett.* **100** (2008) 242001 [arXiv:0802.2470] [SPIRES].

[16] J.M. Butterworth, A.R. Davison, M. Rubin and G.P. Salam, *Jet substructure as a new Higgs search channel at the LHC*, *AIP Conf. Proc.* **1078** (2009) 189 [arXiv:0809.2530] [SPIRES].

[17] D. Zeppenfeld, R. Kinnunen, A. Nikitenko and E. Richter-Was, *Measuring Higgs boson couplings at the LHC*, *Phys. Rev.* **D 62** (2000) 013009 [hep-ph/0002036] [SPIRES].

[18] TEVATRON NEW PHENOMENA, HIGGS WORKING GROUP, G. Bernardi et al., *Combined CDF and D0 upper limits on standard model Higgs-boson production with up to 4.2 fb⁻¹ of data*, arXiv:0903.4001 [SPIRES].

[19] S. Frixione and B.R. Webber, *Matching NLO QCD computations and parton shower simulations*, *JHEP* **06** (2002) 029 [hep-ph/0204244] [SPIRES].

[20] S. Frixione, P. Nason and B.R. Webber, *Matching NLO QCD and parton showers in heavy flavour production*, *JHEP* **08** (2003) 007 [hep-ph/0305252] [SPIRES].

[21] S. Frixione, E. Laenen, P. Motylinski and B.R. Webber, *Single-top production in MC@NLO*, *JHEP* **03** (2006) 092 [hep-ph/0512250] [SPIRES].

[22] S. Frixione and B.R. Webber, *The MC@NLO3.3 event generator*, hep-ph/0612272 [SPIRES].

[23] S. Frixione, E. Laenen, P. Motylinski and B.R. Webber, *Angular correlations of lepton pairs from vector boson and top quark decays in Monte Carlo simulations*, *JHEP* **04** (2007) 081 [hep-ph/0702198] [SPIRES].

[24] S. Frixione, E. Laenen, P. Motylinski, B.R. Webber and C.D. White, *Single-top hadroproduction in association with a W boson*, *JHEP* **07** (2008) 029 [arXiv:0805.3067] [SPIRES].

[25] O. Latunde-Dada, *HERWIG Monte Carlo at Next-to-Leading Order for e⁺e⁻ annihilation and lepton pair production*, *JHEP* **11** (2007) 040 [arXiv:0708.4390] [SPIRES].

[26] P. Nason, *A new method for combining NLO QCD with shower Monte Carlo algorithms*, *JHEP* **11** (2004) 040 [hep-ph/0409146] [SPIRES].

[27] P. Nason and G. Ridolfi, *A positive-weight Next-to-Leading-Order Monte Carlo for Z pair hadroproduction*, *JHEP* **08** (2006) 077 [hep-ph/0606275] [SPIRES].

[28] S. Frixione, P. Nason and G. Ridolfi, *The POWHEG-hvq manual version* 1.0, arXiv:0707.3081 [SPIRES].

[29] S. Frixione, P. Nason and C. Oleari, *Matching NLO QCD computations with parton shower simulations: the POWHEG method*, *JHEP* **11** (2007) 070 [arXiv:0709.2092] [SPIRES].

[30] S. Frixione, P. Nason and G. Ridolfi, *A positive-weight Next-to-Leading-Order Monte Carlo for heavy flavour hadroproduction*, *JHEP* **09** (2007) 126 [arXiv:0707.3088] [SPIRES].

[31] O. Latunde-Dada, S. Gieseke and B. Webber, *A positive-weight next-to-leading-order Monte Carlo for e^+e^- annihilation to hadrons*, *JHEP* **02** (2007) 051 [hep-ph/0612281] [SPIRES].

[32] K. Hamilton, P. Richardson and J. Tully, *A positive-weight Next-to-Leading Order Monte Carlo simulation of Drell-Yan vector boson production*, *JHEP* **10** (2008) 015 [arXiv:0806.0290] [SPIRES].

[33] S. Alioli, P. Nason, C. Oleari and E. Re, *NLO vector-boson production matched with shower in POWHEG*, *JHEP* **07** (2008) 060 [arXiv:0805.4802] [SPIRES].

[34] O. Latunde-Dada, *Applying the POWHEG method to top pair production and decays at the ILC*, *Eur. Phys. J.* **C 58** (2008) 543 [arXiv:0806.4560] [SPIRES].

[35] S. Catani, F. Krauss, R. Kuhn and B.R. Webber, *QCD matrix elements + parton showers*, *JHEP* **11** (2001) 063 [hep-ph/0109231] [SPIRES].

[36] F. Krauss, *Matrix elements and parton showers in hadronic interactions*, *JHEP* **08** (2002) 015 [hep-ph/0205283] [SPIRES].

[37] A. Schalicke and F. Krauss, *Implementing the ME+PS merging algorithm*, *JHEP* **07** (2005) 018 [hep-ph/0503281] [SPIRES].

[38] L. Lönnblad, *Correcting the colour-dipole cascade model with fixed order matrix elements*, *JHEP* **05** (2002) 046 [hep-ph/0112284] [SPIRES].

[39] M.L. Mangano, M. Moretti and R. Pittau, *Multijet matrix elements and shower evolution in hadronic collisions: $Wb\bar{b} + n$ jets as a case study*, *Nucl. Phys.* **B 632** (2002) 343 [hep-ph/0108069] [SPIRES].

[40] S. Mrenna and P. Richardson, *Matching matrix elements and parton showers with HERWIG and PYTHIA*, *JHEP* **05** (2004) 040 [hep-ph/0312274] [SPIRES].

[41] S. Alioli, P. Nason, C. Oleari and E. Re, *NLO Higgs boson production via gluon fusion matched with shower in POWHEG*, *JHEP* **04** (2009) 002 [arXiv:0812.0578] [SPIRES].

[42] A. Papaefstathiou and O. Latunde-Dada, *NLO production of W' bosons at hadron colliders using the MC@NLO and POWHEG methods*, arXiv:0901.3685 [SPIRES].

[43] M. Bähr et. al., *Herwig++ 2.2 release note*, arXiv:0804.3053 [SPIRES].

[44] M. Bahr et al., *HERWIG++ physics and manual*, *Eur. Phys. J.* **C 58** (2008) 639 [arXiv:0803.0883] [SPIRES].

[45] R. Kleiss, *From two to three jets in heavy boson decays: an algorithmic approach*, *Phys. Lett.* **B 180** (1986) 400 [SPIRES].

[46] M.H. Seymour, *A simple prescription for first order corrections to quark scattering and annihilation processes*, *Nucl. Phys.* **B 436** (1995) 443 [hep-ph/9410244] [SPIRES].

[47] J.M. Campbell and R.K. Ellis, *Radiative corrections to $Zb\bar{b}$ production*, *Phys. Rev.* **D 62** (2000) 114012 [hep-ph/0006304] [SPIRES].

[48] S. Dawson, *Radiative corrections to Higgs boson production*, *Nucl. Phys.* **B 359** (1991) 283 [SPIRES].

[49] A. Djouadi, M. Spira and P.M. Zerwas, *Production of Higgs bosons in proton colliders: QCD corrections*, *Phys. Lett.* **B 264** (1991) 440 [SPIRES].

[50] M. Spira, A. Djouadi, D. Graudenz and P.M. Zerwas, *Higgs boson production at the LHC*, *Nucl. Phys.* **B 453** (1995) 17 [hep-ph/9504378] [SPIRES].

[51] S. Catani, D. de Florian and M. Grazzini, *Higgs production in hadron collisions: soft and virtual QCD corrections at NNLO*, *JHEP* **05** (2001) 025 [hep-ph/0102227] [SPIRES].

[52] S. Catani, D. de Florian and M. Grazzini, *Direct Higgs production and jet veto at the Tevatron and the LHC in NNLO QCD*, *JHEP* **01** (2002) 015 [hep-ph/0111164] [SPIRES].

[53] R.V. Harlander and W.B. Kilgore, *Next-to-Next-to-Leading Order Higgs production at hadron colliders*, *Phys. Rev. Lett.* **88** (2002) 201801 [hep-ph/0201206] [SPIRES].

[54] C. Anastasiou and K. Melnikov, *Higgs boson production at hadron colliders in NNLO QCD*, *Nucl. Phys.* **B 646** (2002) 220 [hep-ph/0207004] [SPIRES].

[55] S. Catani and M. Grazzini, *An NNLO subtraction formalism in hadron collisions and its application to Higgs boson production at the LHC*, *Phys. Rev. Lett.* **98** (2007) 222002 [hep-ph/0703012] [SPIRES].

[56] M. Grazzini, *NNLO predictions for the Higgs boson signal in the $H \to WW \to l\nu l\nu$ and $H \to ZZ \to 4l$ decay channels*, *JHEP* **02** (2008) 043 [arXiv:0801.3232] [SPIRES].

[57] . Kramer, Michael, E. Laenen and M. Spira, *Soft gluon radiation in Higgs boson production at the LHC*, *Nucl. Phys.* **B 511** (1998) 523 [hep-ph/9611272] [SPIRES].

[58] B. Mele, P. Nason and G. Ridolfi, *QCD radiative corrections to Z boson pair production in hadronic collisions*, *Nucl. Phys.* **B 357** (1991) 409 [SPIRES].

[59] S. Frixione, P. Nason and G. Ridolfi, *Strong corrections to W Z production at hadron colliders*, *Nucl. Phys.* **B 383** (1992) 3 [SPIRES].

[60] S. Frixione, *A Next-to-Leading Order calculation of the cross-section for the production of W^+W^- pairs in hadronic collisions*, *Nucl. Phys.* **B 410** (1993) 280 [SPIRES].

[61] M.L. Mangano, P. Nason and G. Ridolfi, *Heavy quark correlations in hadron collisions at Next-to-Leading Order*, *Nucl. Phys.* **B 373** (1992) 295 [SPIRES].

[62] S. Catani and M.H. Seymour, *A general algorithm for calculating jet cross sections in NLO QCD*, *Nucl. Phys.* **B 485** (1997) 291 [*Erratum ibid.* **B 510** (1998) 503] [hep-ph/9605323] [SPIRES].

[63] L. Lönnblad, *ThePEG, PYTHIA7, HERWIG++ and Ariadne*, *Nucl. Instrum. Meth.* **A 559** (2006) 246 [SPIRES].

[64] T. Sjöstrand, S. Mrenna and P. Skands, *PYTHIA 6.4 physics and manual*, *JHEP* **05** (2006) 026 [hep-ph/0603175] [SPIRES].

[65] S. Gieseke, P. Stephens and B. Webber, *New formalism for QCD parton showers*, *JHEP* **12** (2003) 045 [hep-ph/0310083] [SPIRES].

[66] A.D. Martin, R.G. Roberts, W.J. Stirling and R.S. Thorne, *NNLO global parton analysis*, *Phys. Lett.* **B 531** (2002) 216 [hep-ph/0201127] [SPIRES].

[67] M.R. Whalley, D. Bourilkov and R.C. Group, *The Les Houches Accord PDFs (LHAPDF) and Lhaglue*, hep-ph/0508110 [SPIRES].

[68] S. Catani, Y.L. Dokshitzer, M.H. Seymour and B.R. Webber, *Longitudinally invariant K_t clustering algorithms for hadron hadron collisions*, *Nucl. Phys.* **B 406** (1993) 187 [SPIRES].

[69] J.M. Butterworth, J.P. Couchman, B.E. Cox and B.M. Waugh, *KtJet: a C++ implementation of the K_T clustering algorithm*, *Comput. Phys. Commun.* **153** (2003) 85 [hep-ph/0210022] [SPIRES].

[70] G. Corcella et al., *HERWIG* 6.5*: an event generator for hadron emission reactions with interfering gluons (including supersymmetric processes)*, *JHEP* **01** (2001) 010 [hep-ph/0011363] [SPIRES].

[71] G. Corcella and M.H. Seymour, *Initial state radiation in simulations of vector boson production at hadron colliders*, *Nucl. Phys.* **B 565** (2000) 227 [hep-ph/9908388] [SPIRES].

[72] M.H. Seymour, *Matrix element corrections to parton shower algorithms*, *Comp. Phys. Commun.* **90** (1995) 95 [hep-ph/9410414] [SPIRES].

[73] D. de Florian, M. Grazzini and Z. Kunszt, *Higgs production with large transverse momentum in hadronic collisions at Next-to-Leading Order*, *Phys. Rev. Lett.* **82** (1999) 5209 [hep-ph/9902483] [SPIRES].

[74] G. Davatz et al., *Combining Monte Carlo generators with Next-to-Next-to-Leading order calculations: event reweighting for Higgs boson production at the LHC*, *JHEP* **07** (2006) 037 [hep-ph/0604077] [SPIRES].